Optical Properties of Anatase and RutilePhase TiO₂ Nanotubes

by

Yun Zhang

A thesis submitted in partial fulfillment of the requirements for the degree of

Master of Science
in
Microsystems and Nanodevices

Department of Electrical and Computer Engineering
University of Alberta

Abstract

Nanofabricated optically anisotropic uniaxial thin films with deep submicron feature sizes are emerging as potential platforms for low-loss all-dielectric meta-materials and for Dyakonov surface wave-based sub-wavelength optical confinement and guiding at interfaces with isotropic media. In this context, we fabricated anatase and rutile phased titania nanotube arrays (TNTAs) and investigated the optical properties of one such uniaxial platform, namely self-organized TNTAs grown by the bottom-up nanofabrication process of electrochemical anodization on silicon wafer substrates. Transmittance spectra measurement was used to investigate the isotropic properties of TNTAs, and refractive index was extracted from the spectra fringes. Variable angle spectroscopic ellipsometry was used to investigate the optical anisotropy in two phases of TNTAs. One phase is anatase and the other phase contains a mixture of anatase and rutile. Both kinds of TNTAs were found to have positive birefringence (Δn). The experimentally measured anisotropy in the refractive index of the TNTAs was compared with model-predictions of two different effective medium approximations incorporating the uniaxial geometry. The measured value of Δn for anatase-phase TNTAs exceeded that of bulk anatase single crystals, indicating the potential of nanostructured dielectrics to outperform dielectric crystals of the same material with respect to the magnitude of the achievable directional refractive index contrast.

Preface

The dissertation is submitted for the degree of the Master of Science at the University of Alberta. This Master thesis contains resultsof the research undertaken inthe Department of Electrical and Computer Engineering, University of Alberta, from July 2013 to July 2017, under the supervision of Professor Karthik Shankar.

The fabrication and characterization work in the chapter 2 was mainly performed by me with the equipment in our lab and the nanoFAB under the guidance of Prof. Karthik Shankar, and Dr. PiyushKar. The main content of this chapter has been published as Kar, P., Zhang, Y., Farsinezhad, S., Mohammadpour, A., Wiltshire, B.D., Sharma, H. and Shankar, K., 2015. *Rutile phase n-and p-type anodic titania nanotube arrays with square-shaped pore morphologies*. Chemical Communications, 51(37), pp.7816-7819.

Chapter 3 of this thesis was the work done by myself with the equipment in our lab and the nanoFAB under the guidance of Prof. Karthik Shankar.

Chapter 4 of this thesis has been publishedas Zhang, Y., Farsinezhad, S., Wiltshire, B., Kisslinger, R., Kar, P. and Shankar, K., 2017. *Optical anisotropy in vertically oriented TiO2 nanotube arrays*. Nanotechnology, 28(37).

Acknowledgements

My master student life would never have reached its culmination without the people who have generously helped me over the past four years. I would like to thank all the people who contributed in some way to the work described in this dissertation. I feel privileged to express my thanks to them for their support, assistance and encouragement.

Foremost, I want to express my deep thanks to my supervisor Dr. Karthik Shankar, whom I also regard as my most respectful teacher and wise friend. His unreserved guidance and patience has led me through barriers and the struggles during my research. His continuous encouragement and guidance always help me to move forward. His profound instruction for both academic and life will definitely help me a lot in my future career. My appreciations also go to the rest of my committee, Professor Hyun-Joong Chung and Professor Ray DeCorby.

All the results described in this thesis was accomplished with the support and help of my labmates. I was greatly benefited from their keen scientific insight in every group discussion. The ideas can always inspire new thoughts in my mind and help me solve the problems. My deepest thanks go to my colleagues: AbdelrahmanAskar,AhmadAdl, ArashMohammadpour, ArezooHosseini, Ben Wiltshire, MouradBenlamri, Najia Mahdi, Ryan Kisslinger, Samira Farsinezhad, Sheng Zeng, Ujwal Kumar Thakur, and WeidiHua.Thanks for all the good times we spend together and it would definitely be existing in my memory forever.I would like to deliver my special appreciation to Dr. PiyushKar who is my co-supervisor and helped me a lot in both my research work and

Table of Contents

List of Figures

Figure 1- 6 (a) the refractive index and extinction coefficient bulk anatase, rutile, and thin-film anatase determined from the spectroscopic ellipsometry data. (b) optical functions of bulk. Top, real and imaginary parts of the complex refractive index for the ordinary and the extraordinary directions; bottom, absorption coefficients for the ordinary

List of Tables

List of Symbols

n	Refractive Index
n*	Complex refractive Index
n_o	Ordinary refractive Index
n_e	Extraordinary refractive Index
Δn	Birefringence
k	Extinction Coefficient
ε_o	Ordinary permittivity
ε_e	Extraordinary permittivity
$\varepsilon_{eff}^{\parallel}$	Effective permittivity parallel to the cylinder axis
$\varepsilon_{eff}^{\perp}$	Effective permittivity perpendicular to the cylinder axis
λ	Wavelength
α	Full-width at half maximum in XRD peak
θ	Bragg angle
I_a	Peak intensity in XRD patterns of anatase
I_r	Peak intensity in XRD patterns of rutile
p	Percentage of rutile
ΔE	Full-width at half maximum in Raman peak
vol%	Volume percentage
wt%	Weight percentage
s	Refractive index of substrate
T	Transmittance
T_M	Transmittance interpolated by maximum envelope

T_m	Transmittance interpolated by minimum envelope
d	Film thickness
M	Number of peaks in reflection measurement
f	Volume fill fraction
a	Outer radius of the nanotubes
b	Inner radius of the nanotubes
β	Center-to-center spacing of the nanotubes
r_s, r_p	Fresnel reflection coefficients for s- and p- polarized light
Ψ	Ellipsometric amplitude parameter
Δ	Ellipsometric phase parameter

List of Abbreviations

TNTAs	titania nanotube arrays
TiO_2	titanium dioxide
CO_2	carbon dioxide
ZnO	zinc oxide
Au	gold
TiN	titanium nitride
HF	hydrofluoric acid
CH3COOH	acetic acid
EG	ethylene glycol
NH_4F	ammonium fluoride
1-D	one dimensional
HANTs	high temperature annealed nanotubes
LANTs	low temperature annealed nanotubes
FANTs	flame annealed nanotubes
NWAs	nanowire arrays
FWHM	full width at half maximum
FESEM	scanning electron microscopy
UV-Vis-NIR	Ultraviolet-visible-near infrared
XRD	x-ray diffraction
VASE	variable angle spectroscopic ellipsometry
AOI	angle of incidence

EMA	effective medium approximation
BR	Bruggeman
MG	Maxwell-Garnett
CYL	cylindrical
ALD	atomic layer deposition

Chapter 1.   Introduction[2]

This thesis concentrates on the study of morphological, optical, and electrical properties of rutile phase titania nanotube arrays (TNTAs) formed by annealing of anatase phase TNTAs in air or in a propane flame with temperature modification. This will introduce the application of TNTAs based on its optical properties and illustrate the fabrication of rutile phase TNTAs where the processes of electrochemical anodization and conditioned annealing will be demonstrated. The ellipsometry technique by which the optical properties of TNTAs are measured will be explained in details as well.

1.1   Introduction to TiO_2

Titanium Dioxide (TiO_2), also known as titania, is the only naturally occurring oxide of titanium at atmosphere pressure[1-2].The elements of Ti an O are rich in earth crust, and $TiO_2$is chemically stable, which resulting TiO_2a relatively inexpensive material. The three polymorphs of titania are anatase, brookite and rutile[2].Both anatase and rutile have tetragonal crystal structures, and brookite has orthorhombic crystal structure, as shown inFigure 1- 1. Rutile has two formula units in its unit cell. In rutile unit cell, a = b = 4.5937 Å and C = 2.9537 Å. Anatase has four formula units in its unit cell. In anatase unit cell, a = b = 3.7845 Å and C = 9.5143 Å[3].Basic unit of TiO_2 of both anatase and rutile is a distorted octahedron comprising of a central Ti atom and surrounding oxygen atoms. Ti atoms are coordinated with 6 oxygen atoms, the oxygen atoms are coordinated at 3 titanium atoms. One of the Ti-O bond is longer than the others. TiO_6 units in rutile

are connected by edge-sharing. The oxygen in the edge-shared TiO_6 in rutile is corner-shared with other oxygen atom. Anatase TiO_6 units have corner-shared oxygen atoms in the (001) plane, whereas adjacent (001) planes are connected by edge-sharing. TiO_2 is known to be applicable in a range of important technological areas, including semiconductors, optical devices, photovoltaic cells, catalysts, gas sensing, and electrochemical storage.
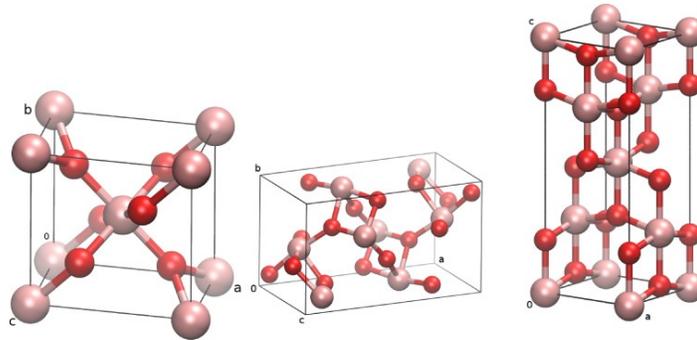
Figure 1- 1Titanium dioxide crystal structures of rutile, brookite and anatase (from left to right). Reprinted from[4]with permission from IOP Publishing Ltd.

The anatase polymorph of TiO_2 occurs naturally and is found in earth's crust, although less abundantly than the rutile polymorph of TiO_2. Anatase has a bandgap of 3.2 eV, has an optical absorption edge of about 350 nm, and its mainly yellow in color.AnataseTiO_2 crystallizes from the amorphous state of TiO_2 at about 400^oC. The predominant crystalline plane of anatase is the (101), as observed clearly in X-ray diffraction patterns. Among the various applications of anatase TiO2 are biomedical implants[5], coatings[6], paints[7], food products and light driven energy conversion applications that include photovoltaic and photocatalysis. Anatase has been reported to have the highest photoactivity among all three titania[8-10].Considering these existing

applications and potentialfor the new applications, particularly in the realm of photocatalysis and photovoltaic, the anatase polymorph of TiO_2 has attracted considerable interest over the last three decades. Even though anatase TiO_2 is a technology sought-after material for researchers working solar cells and solar photovoltaics, its large bandgap renders it photoactive under ultraviolet radiation, and therefore it can only 4% of the solar spectrum. To address this and other issues problems such as susceptibility to poisoning of surface under photocatalytic reactions[11], research focus is on other materials and also the rutile polymorph of TiO_2.

Rutileis the most commonpolymorph of TiO_2. It has higher refractive index than anatase and hence is preferably used in interference applications[12-13]. It is also hard and has chemical resistant properties. When viewed by transmitted light, the rutile exhibits a deep red color. Powdered form of rutile serves as white pigmentation for paints, paper, plastics, foods and other objects which need a white color[13].Nanoscale rutile particles are also used for the effective absorption of ultraviolet rays[14].With this characteristic, rutile is mixed to produce sunscreens and to prevent skin damage.Rutile is the stable crystalline phase of TiO_2 with a predominant plane of (110) appearing in its X-ray diffraction pattern, whereas anatase and brookite are metastable and are readily transformed to rutile when heated. Given its strong chemical resistance, in strong acidic and basic conditions, rutile has been used in dye-sensitized solar cells[15] and lithium batteries extensively[16]. In spite of superior performance of rutile TiO_2 in many applications, including through related light harvesting and energy conversion,it has received less attention and exploration than anatase[17].In addition to pure rutile phase

there is growing interest in mixed rutile and anatase crystalline phase TiO_2 nanotubes, for analyzing enhancement of performance in various leading edge applications[18].

Brookite is the least studied polymorph of TiO_2 due to its instability and difficulties in synthesizing a pure phase. The brookite crystalline phase is a biaxial optical material with very high refractive index, i.e. between 3.5 and 3.7. The bandgap of brookite is 1.9eV[19]. The lack of focus of researchers on brookite is because of its instability[20].

1.2 TiO_2 nanotube arrays (TNTAs) and the motivation to use them

Today, the three major trends in nanotechnology are pictorially depicted in Figure 1-2, and are anodic formation of ordered arrays of 1-D nanostructures (i.e. nanotubes, nanowires and nanorods), non-lithography nanofabrication, and template enabled growth of 1-D semiconductors. Since TNTAs lie at the intersection of the three trends, it has gained enormous interest with more than a thousand related papers published over the last ten years[21].
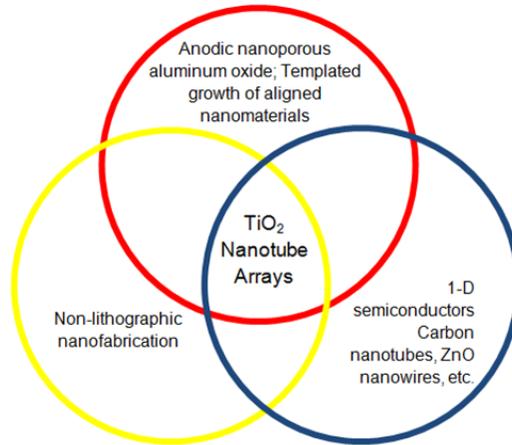
Figure 1- 2TNTAs sit at the intersection of three major nanotechnology trends. Edited and reprinted from [21] with permission from Springer Netherlands.

TNTAs are emerging as functional materials for application in gas sensing, piezoelectric, dielectric devices, photochromic materials, light harvesting devices (photocatalysis and photovoltaics) and charge storage devices such as supercapacitors. The domain of application of TNTAs is enhanced because of their: tubular 1-D nanostructure morphology that can be easily tuned to various aspect ratios, and tube wall thicknesses [22]; their adaptability to bandgap engineering by simple doping process; compatibility with surface functionalization methods; and controllable carrier concentration and crystalline phase composition by application of simple annealing methods.

TNTAs are used in light harvesting devices, particularly because they are uniaxial nanostructures. One major limitation on light harvesting devices efficiency is due to its trade-off between charge generation and light absorption, as well as between charge

separation and carrier collection. The uniaxial nanostructure of TNTAs allows the two processes to occur in orthogonal directions. Charge separation now occurs in the radial direction while light absorption occurs in the longitudinal direction of nanotubes. The porous structure of TNTAs also enhances the light absorption efficiency due to scattering effects. As a result, it is possible to fabricate TNTAs based for solar cells with higher photoconversion efficiency [23].Similarly, it is possibly to tune to bandgap of TNTAs to extend the optical edge, which can aid in photocatalysis applications. Photocatalytic CO_2reduction is another area where TNTAs are used, which requires anoptimal band gaps for light harvesting and band-alignment for facilitating chemical reactions. TNTAs and functionalization of the same are being researched extensively on this front. Optical biosensors operate on surface functionalization that TNTAs and subsequently using a fluorescent dye that can be detected if the dye is tagged to biomarkers. Optical biosensors based on TNTAs can also be made using the high refractive index that would contrast the refractive of the biomarkers[24]. High performance super-capacitors can be fabricated using surface area of TNTAs[25].

TNTAs generally pertain to anatase crystalline phase of TNTAs. These have been widely researched, and are being been manufactured commercially, but not many research reports exist on rutile crystalline phase of TNTAs even though there are examples of better performance of rutile phase TNTAs than anatase phase TNTAs. Figure 1- 3 shows better photoelectrochemical water splitting performance by our flame annealed rutile phase TiO_2 nanotubes (FANTs), and by high temperature annealed rutile phase TNTAs (HANTs) than conventionalanatase phase TNTAs (or LANTs)[26].This thesis serves to fill that void in literature. Anatase phase is known to transform to rutile

phase by raising annealing temperatures beyond 500 ºC but balance of annealing time and temperature, as well as methodologies greatly affect the morphologies of TNTAs and their crystalline phase content. As mentioned in Chapter 2, rutile phase TNTAs can be formed by flame annealing and also by high annealing under controlled conditions. Details about conditions for rutile phase formation and characterization of the resulting TNTAs are discussed in details in Chapter 2 of this thesis.
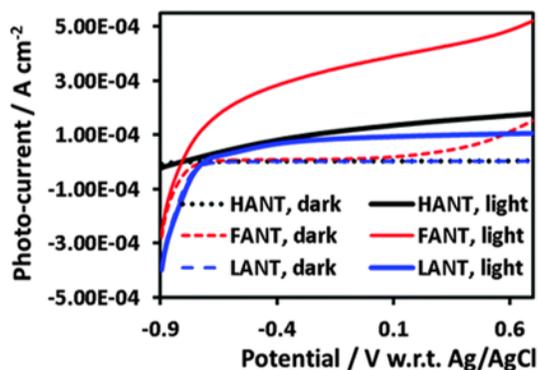
Figure 1- 3Photoelectrochemical water splitting performance by rutile and anatase TNTAs. Reprinted from [26] with permission from Royal Society of Chemistry.

1.3   Optical properties of TNTAs

TNTAs have received intense interest among researchers because of their technological importance, as stated above, which are, to a large extent, associated with their optical properties that can be engineered according to applications of interest. For example, refractive index of TNTAs and the variation of the same, can affect

performance of refractive index based biosensors. Similarly, light absorption and transmission characteristics of TNTAs can affect performance of TiO_2 based solar cells.
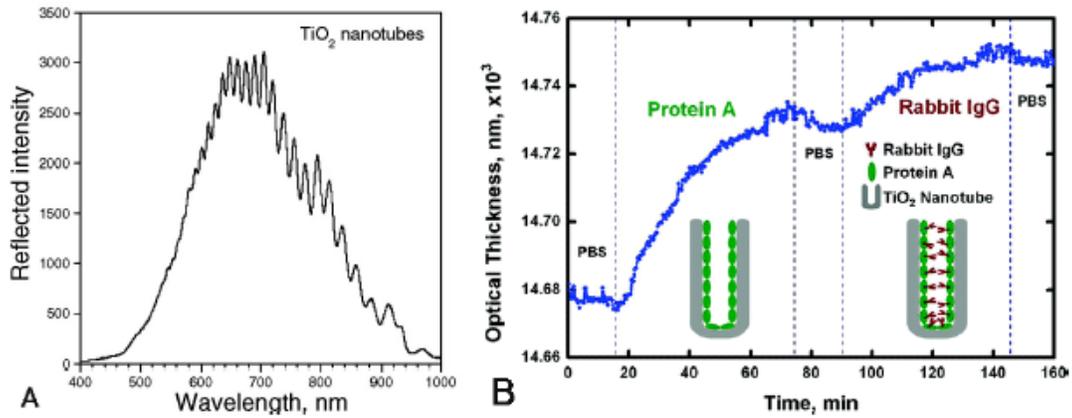
Figure 1- 4TNTA-based interferometric biosensors: (A) representative reflectivity spectrum of anodic TNTAs showing the characteristic interference fringes and (B) Time-dependent optical thickness measurements showing sequential binding of Protein A and rabbit IgG within TNTAs. Reprinted from [27] with permission from Springer Netherlands.

Refractive index, of anodically formed self-organized TNTAs fabricated on Kapton were reported by Samira et al.[28].The periodic pattern of interferometric fringes in transmission spectra of the TNTAs were used to determine the isotropic wavelength-dependent refractive indices and film thickness of TNTAs. Similar work has been done by G.K. Mor et al.[29],where they reported (as shown in Fig. 1-5) characterization results of TNTA that were prepared on glass substrates.Kapton has small optical thickness and it strongly absorbs light of wavelength smaller than 500 nm. Therefore, with Kapton substrate there is a likelihood of existence of interferometric fringes, which compromises

accuracy of the measurement. On the other hand, refractive index of TNTAs, in Mor's work as well as in Chapter 3 of this thesis, TNTAs are fabricated on undoped glass, where interferometric fringes are ruled out.
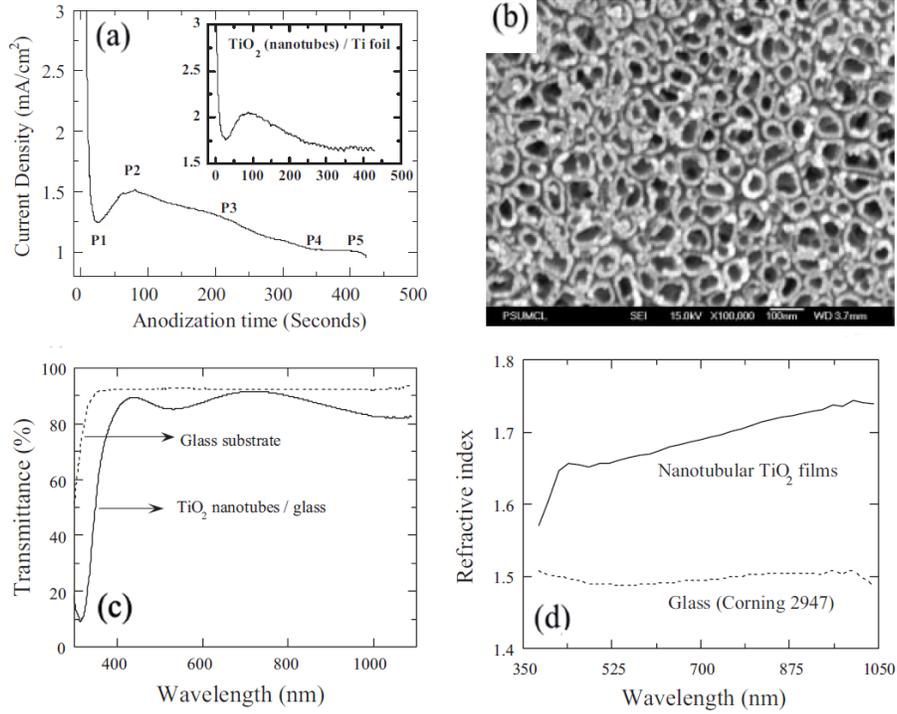
Figure 1- 5 A 400 nm Ti film on glass was formed by sputtering and subjected to electrochemical anodization in a 1% HF electrolyte at 10V to form TiO_2 nanotube arrays. (a) Anodization current versus time (b) top view FESEM image showing the surface of TiO_2 nanotube arraysgrown from a 400nm thick Ti thin film (c) optical transmittance of glass substrate and450°C annealed TiO_2 nanotubes atop the same glass and (d) effective refractive index of the nanotube arrays on glass, calculated by applying the envelope to the transmission spectra as shown in the inset. Reprinted from [29] with permission from John Wiley & Sons, Inc.

Moreover, materials with uniaxial symmetry exhibit anisotropic optical properties. i.e. they have two distinct refractive indices (or extinction coefficients) dispersion with

wavelength. The ordinary refractive indices, n_o, (or extinction coefficients, k_o) are used to describe light interactions for light polarized perpendicular to the optical axis, while The extraordinary refractive, n_e, (or extinction coefficients, k_e) are used to describe light interactions for light polarized parallel to the optical axis.

TNTAs are anisotropic nanostructured materials due to two factors, their crystal structure and morphology. The former reason can be expressed from the fact that both anatase and rutile crystals have tetragonal symmetry. Such uniaxial structure caused anisotropic optical properties have been reported by G. E. Jellison, Jr. et al.[12-13] as shown in Figure 1- 6. Clearly both anatase and rutile crystals show significant anisotropy and birefringence ($\Delta n = n_e - n_o$) of rutile is greater that of anatase.
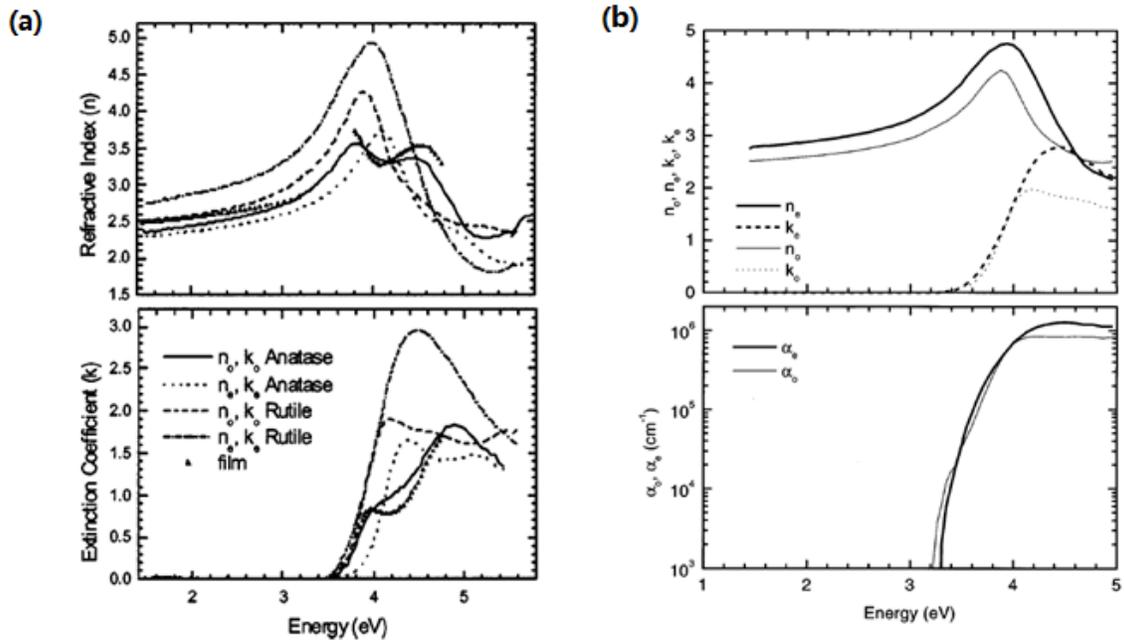
Figure 1- 6 (a) the refractive index and extinction coefficient bulk anatase, rutile, and thin-film anatase determined from the spectroscopic ellipsometry data. (b)optical functions of bulk. Top, real and imaginary parts of the complex refractive index for the ordinary and the extraordinary directions; bottom, absorption coefficients for the ordinary

and the extraordinary directions. Reprinted from[12-13] with permission from IOP Publishing Ltd, and Optical Society of America.

The latter reason lies on its uniaxial tubular morphology. Figure 1- 7 shows an example of the morphology of TNTAs formed on native substrates. When light propagates along the longitudinal direction of nanotubes, the tubular structure becomes a waveguide which confines the light propagation within the high dielectric constant material. Hence, the refractive index with light incident along the optical axis is supposed to be higher than the refractive index with light incident perpendicular to the optical.
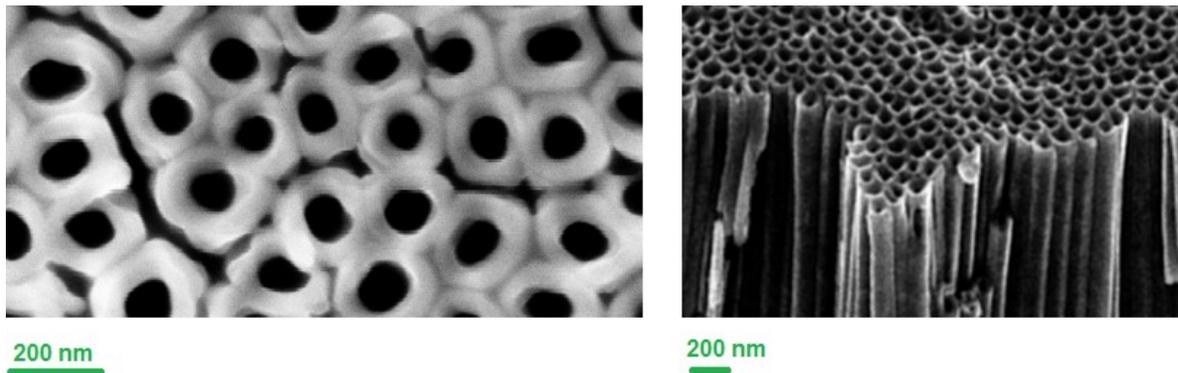
Figure 1- 7Top view (left) and cross section (right) of TNTAs on native substrate.

Unfortunately, the anisotropic optical properties of TNTAs have never been discovered. However, optical anisotropy of some metal oxides with one dimensional nanostructure similar to TNTAs has been discovered in a few researches. In 2011, Cheng-Ying Chen et al. discovered the anisotropic optical properties of ZnO nanowires with reflection spectroscopy[30].Their Fresnel reflection in multiple layers was used forquantitative analysis[31-34], and is shown in Figure 1- 8and Figure 1- 9. It is obvious

that ZnO nanowires show significant optical anisotropy due to its one dimensional nanostructures.
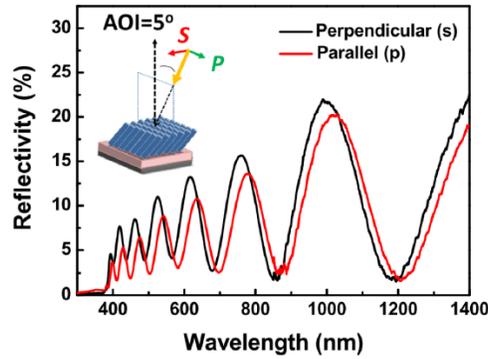
Figure 1- 8 Reflectivity spectra of the oblique-aligned ZnO NWAs for s- and p-polarization at the AOI of 5°. The plane of incidence is aligned to the orientation of NWs. The s- and p-polarization is perpendicular and parallel to the azimuthal direction of the long axis of obliquealigned NWAs, respectively. Reprinted from [30] with permissionfrom Optical Society of America.
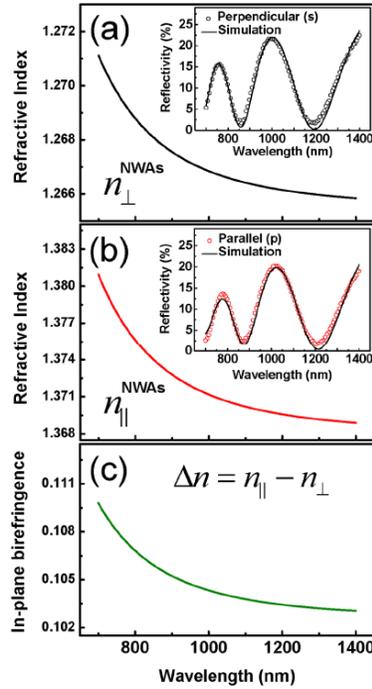
Figure 1- 9 Determination of the equivalent reflective index dispersion curve of the oblique-aligned ZnO NWAs for the polarization (a) perpendicular and (b) parallel to the azimuthal direction of the long axis of oblique-aligned NWAs. (c) The in-plane birefringence of the oblique-aligned ZnO NWAs. The insets of (a) and (b) are the comparison of simulated and experimental reflectivity spectra of the NWAs on the ZnO buffer layer/Si substrate. Reprinted from[30] with permission from Optical Society of America.

Since their tubular morphology caused optical anisotropy has not been discovered yet, this thesis will used to reveal the uniaxial optical properties of TNTAs with the ellipsometry techniqueto fill the vacancy.

1.4   Outline of the thesis

In this thesis, we focus on the anisotropic optical properties of mixed anatase and rutile phase TNTAs with uniaxial tubular nanostructures. A comprehensive study is made from both experimental and data analysis works.

Chapter 1 introduces the structural properties of TiO_2 and various applications of both bulk TiO_2 and TNTAs. Some previous studies on the optical properties of TNTAs and other optically anisotropic materials are described in details.

Chapter 2 presents the processes for fabricating TNTAs by electrochemical anodization, and the methods applied for annealing to attain desired crystalline phase. The chapter also discusses about characterization of TNTAs by XRD and Raman spectroscopy.

Chapter 3 presents the isotropic optical properties of TNTAs fabricated on glass. The Swanepoel's method for analyzing transmittance spectra was demonstrated in this chapter.

Chapter 4 presents the isotropic optical properties of TNTAs fabricated on silicon. The experimental work with the WVASE ellipsometer and ellipsometry data model fitting are exhibited in details in this chapter.

Chapter 5 is a summary of the work done towards this thesis, as presented in chapters 2 to 4. The chapter also mentions the future work on similar nanostructured materials that can be built upon the methodologies and findings of this thesis.

Chapter 2.   Fabrication and characterization of rutile containing TNTAs

In this chapter, I describe the electrochemical anodization and annealing methods applied to fabricate rutile phase containing TNTAs on Ti foil, as well as those on Si substrate. Thereafter, I discuss the characterization methods of the annealed TNTAs by field emission scanning electron microscopy (FESEM), x-ray diffraction (XRD) and Raman spectroscopy.

2.1   Electrochemical Anodization

TNTAs can be synthesized by a number of methods, including use of nanoporous alumina templates[35], hydrothermal techniques[36], and electrochemical anodization. With the first method, the dimensions of nanotubes can be controlled by modification of alumina templates parameters, but limitations exists in that it can hardly synthesize small-sized and yet smooth nanotubular structures[37]. The hydrothermal technique can be used to make small diameter nanotubes but highly ordered TNTAs are not possible by this method[38]. The electrochemical anodization technique addresses the deficiencies in the above two methods, and therefore it is the most widely used method for fabricating ordered arrays of TNTAs. Electrochemical anodization technique draws its strength from superior control over the key parameters that affect the morphologies and dimensions of the nanostructures. These parameters include: electrolyte viscosity, composition as well as concentration; anodization potential and time; mode of DC bias (i.e. constant current

or constant voltage); and simplicity of operation. Details about principles of Ti anodization processes are well documented in literature [29, 39-40]. Amorphous TNTAs can be then transferred into anatase and rutile phase by applying annealing in different conditions. The processes of electrochemical anodization and annealing are discussed in sections 2 and 3 of this chapter.

2.2 Mechanism of the growth of TNTAs by electrochemical anodization

The electrochemical anodization of TNTAs occurs as a result of four competing processes, which are: field assisted oxidation, field assisted migration, field assisted dissolution, and chemical dissolution, see in Figure 2- 1. In the both organic and aqueous electrolytes, water provides the reactants, O^{2-} or OH^{-} ions which react with Ti^{4+} that are released from the anode. This results in the formation of anhydrous and hydrated oxides by reactions:

$$Ti^{4+} + 2O^{2-} \rightarrow TiO_2 \qquad (1)$$

$$Ti^{4+} + 4OH^{-} \rightarrow Ti(OH)_4 \qquad (2)$$
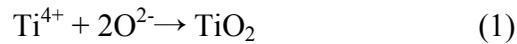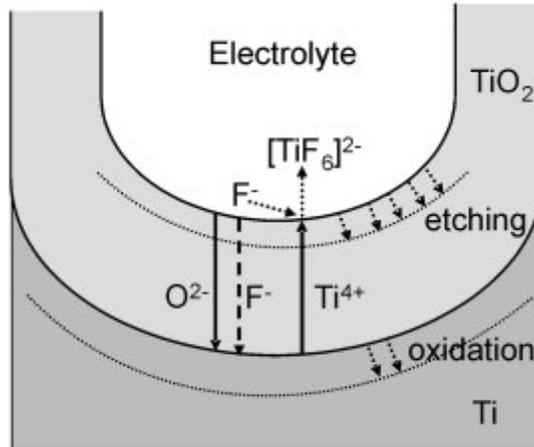
Figure 2- 1 Illustration of the anodic TNTAs growth in presence of fluorides. Reprinted from[41] with permission from Elsevier.

Previous studies showed that there is a hydration concentration gradient across the film during anodization, a $TiO_2.xH_2O$ complex is presented as the product, wherethe outer anodic layer of which has more hydroxyl ions that forms a $Ti(OH)_4$ hydrated layer while the inner layer is anhydrous with TiO_2[42-43].

Both TiO_2 and $Ti(OH)_4$ can be chemically dissolved by fluoride ions, known as chemical dissolution:

$$TiO_2 + 6F^- + 4H^+ \rightarrow [TiF_6]^{2-} + 2H_2O \qquad (3)$$

$$Ti(OH)_4 + 6F^- \rightarrow [TiF_6]^{2-} + 4OH^- (4)$$
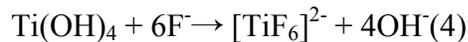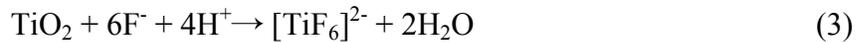
In addition, the presence of electrical field can also weaken the bond between Ti and O, known as field assisted dissolution:

$$TiO_2 + 6F^- + 4H^+ \rightarrow [TiF6]^{2-} + 2H_2O \qquad (5)$$
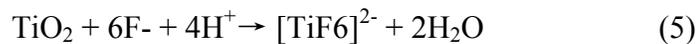
The field assisted etching process leads to the pore initiation at the oxide/electrolyte interface[44-45].There is a plastic flow of oxides towards the cell boundaries by a flow mechanism being responsible to form a fluoride rich layer which triggers the pore to tube

transition. Su and Zhou[46]also show that the dehydration of$TiO_2.xH_2O$ formed on the outer wall.

Under the assistance of applied potential the fluoride ions flow towards the anodic metal and Ti^{4+} ions flow towards the electrolyte. Such process leads the formation of fluoro-complexes among which $[TiF_6]^{2-}$ is the most stable in the electrolyte.

Thesereactionsleadto threestagesofTiO_2 nanotube growth, as shown inFigure 2- 2, whereby the anodization current density changes with time. The first stage is when the anodization process begins and current density experiences a sudden drop because of diffusion limitation on reactants (O^{2-} or OH^- ions) imposed by the produced barrier layer. The second stage is where current density increases,since more ion migration paths are created by the formation of the porous or tubular structures. The field assisted and chemical dissolution of barrier layer, whereby the fluoride ions etch TiO_2 forming titanium hexafluoride. These dissolution processes lead to the decrease of film resistance decreases causing the current density to increase. The etching process comprises of reaction of fluoride ions with the oxide layer, and formation of pores on the oxide layer.The third stage is where the etching process continues under the influence of electric field wherein the fluoride ions simultaneously diffuse through the oxide layers and react with it, forming TiO_2 nanotubes. Current density increases slowly during the tube formation process. It is notable that the while oxide formation and etching process occur simultaneously, and in the final stage where the competition between the oxide layer formation and dissolution reaches a steady state, the current density attains a constant value or slow drop.
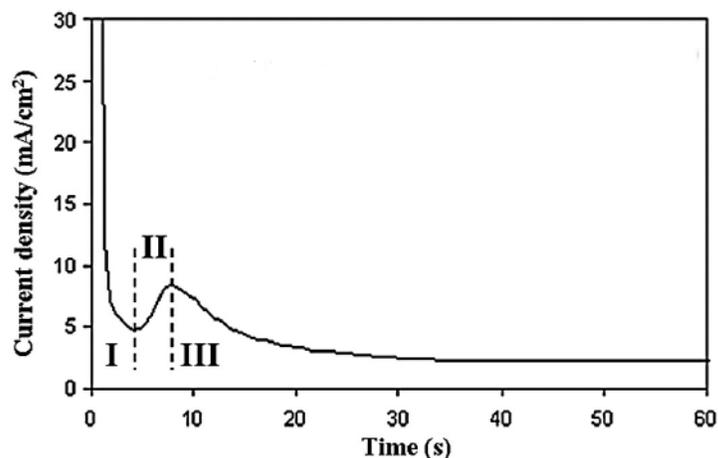
Figure 2- 2 The current-time relation plot for titanium anodized at 20 V. Reprinted from[47]with permission from Wiley-VCH.

2.3   Electrochemical Anodization of Ti foils and Ti deposited on Si substrates

TNTAs on Ti foils were grown by anodization cleaned Ti foil pieces of 1 cm width and 4 cm length. The cleaning of foil was performed by immersion in ultrasonic bath containing detergent and water. Thereafter the Ti foils were rinsed in de-ionized water. Anodization was performed in aqueous electrolytes containing 1% (by volume) HF (hydrofluoric acid), 8% (volume) CH_3COOH (acetic acid). The electrochemical consisted of Ti foils as anode and graphite as cathode, which was 0.3 cm in diameter and 4 cm in length. The spacing between the electrode was maintained at 4 cm. Electrochemical anodization was performed by application of a DC voltage (by using a DC power supply) of 15 V for one hour at room temperature.

To fabricate the TNTAs on Si substrate, a Ti deposition step was involved, wherein, 250 nm-thick Ti (purity >99.999%) films were deposited on to piranha-cleaned n-type <111> oriented Si wafers in a planar DC magnetron sputtering system. The deposition

conditions used were designed to maximize film smoothness by recourse to atomic peening[28]. TNTAs were fabricated by anodization of Ti thin films in ethylene glycol (EG)-based organic electrolyte containing 0.09M (0.3wt %) NH_4F and 9vol% deionized water at a voltage of 40V vs. agraphite counter-electrode placed at a distance of 2cm from the anode. Following anodization, the residual electrolyte and debris were removed by rinsing the samples with methanol.

Figure 2- 3 is the process flow that lists, in step-wise (from top bottom) format, the processes involved in the anodic formation of TNTAs on Ti foil and Si substrate. Anodization is followed by annealing. Details about annealing are discussed in the next section.

Sample (Ti foil and/or Ti sputtered on Si) cleaning and sizing

↓

Preparation of anodization electrolyte, generally a fluoride ions containing aqueous or organic solvent

↓

Placement of sample in a two-electrode electrochemical cell containing the sample as anode and graphite as the cathode

↓

Adjustment of voltage (if constant voltage method) or current (if constant current method) and performing the anodization

↓

Sample drying in air and post-anodization cleaning of debris

↓

Annealing in one the processes: annealing at 450 °C for 2 hours (or desired time), annealing at 450 °C for 30 minutes followed by propane flame annealing; and annealing at 750 °C for 2 hours

Figure 2- 3Process flow for fabrication of anodic TiO_2 nanotubes followed by appropriate annealing procedure.

2.4   Annealing of TNTAs

Annealing induces crystallinity in TNTAs, which in the as-formed or post-anodization stage are amorphous. Normal annealing temperatures can be varied between 300 ~ 750 °C [48]to form anatase phase of TNTAs[49-50]. There is a tradeoff between annealing temperature and annealing time, in that the lower the temperature is the longer is the required time to obtain crystallinity. After the desired annealing temperature is reached the TNTAs are kept at that temperature for a period of time, typically 2.5 hours

[48].Full crystallinity is normally achieved at 300 °C[51].As shown in Figure 2- 4, anatase starts forming at280 ºC, while rutile phase starts forming at400 ºC, however very small percentages of rutile are found at temperature below 600 ºC[52].Although temperatures in excess of 600º C favor rutile phase formation, different nanotube types (as determined from their anodization electrolytes, i.e. aqueous, organic, etc.) may undergo different degree of rutile phase crystallinity. My findings, reported in this thesis, demonstrate that aqueous TNTAs undergo full rutile phase crystallinity at 750 ºC annealing in air and also flame annealing, whereas ethylene glycol based TNTAs undergo partial crystallinity to rutile[53].Details can be found in characterization section of this chapter. There are also literature reports about high temperature annealing of TNTAs, whereby rutile phase of varying degrees are formed and nanotubular morphology is also preserved [40].

In addition to temperature, another important annealing parameter is rate of cooling and heating. Control of heat and cooling rate also has an effect on crystalline defect densities. Generally, the heating rate applied is 200°C per hour and the TNTAs are left to cool overnight. Typically, annealing is performed in an atmosphere of oxygen or air to form phase pure anatase having low oxygen vacancies.If annealing is performed in nitrogen atmosphere, TNTAs with high charge carrier concentration (and high n-type conductivity) are obtained because of presence of oxygen vacancy sites that are rich in electrons. Oxygen and air annealing, on the other hand tend to annihilate the oxygen vacancy defects and diminish the n-type nature of TNTAs. In another variation of annealing atmosphere, if annealing is performed under exposure to hydrogen, black TNTAs are obtained, because they have an extended optical absorption edge. The

annealing process of TNTAs is generally carried out in an oven or in a tube furnace where environment can be controlled by flow of the desired gas. Annealing can also be performed by other methods, such as placement of TNTAs on a hotplate or by use of an appropriate flame. The process flow for formation of TNTAs and thereafter the annealing of the same by various methods is shown in Figure 2- 3, as shown in the figure the annealing process is branched into choice of heating and atmosphere conditions as well as choice of methods used for annealing. In practice, annealing of TNTAs is carried out under strict adherence to process control, which is tuned to the requirement of the type of TNTAs.
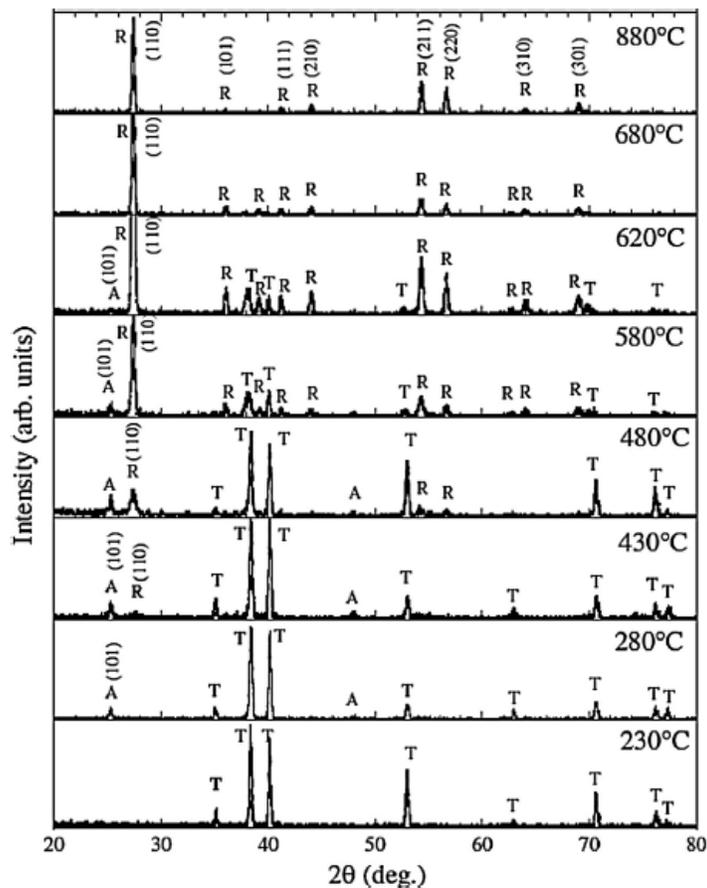
Figure 2- 4 Glancing Angle X-Ray Diffraction (GAXRD) spectra of TNTAss annealed at temperatures ranging from 230 to 880 $^{\circ}$C in dry oxygen. A, R and T indicates anatase, rutile and titanium (substrate), respectively. Reprinted from [52] with permission from Materials Research Society.

2.4.1 Propane flame annealing

In order to fabricate different morphologies of rutile phase TNTAs, we used a two-step annealing procedure. The first step was a furnace annealing process, where the TNTAs were heated to 450 °C and kept at that temperature for 30 minutes. Thereafter, a propane flame instead of furnace was used for the annealing process to raise the temperature of the TNTAs to temperatures above 700 °C. Figure 2- 5, schematically

illustrates the propane flame annealing process for forming rutile phaseTNTAs. The TNTAs on foil that I anodized using aqueous electrolytes were used for propane flame annealing. In the flame annealing process, TNTAs underwent full transformation from anatase to rutile phase, as shown in XRD patterns (discussed in the characterization section of this chapter). Essentially the propane flame annealing process resulted in instantaneous heating of the TNTAs to temperatures higher than 700 °C. By sudden exposure to those temperatures from room temperature, rapid and irreversible phase (from anatase to rutile) andshape change of the TNTAs (from pseudo-circular to square) occurred.
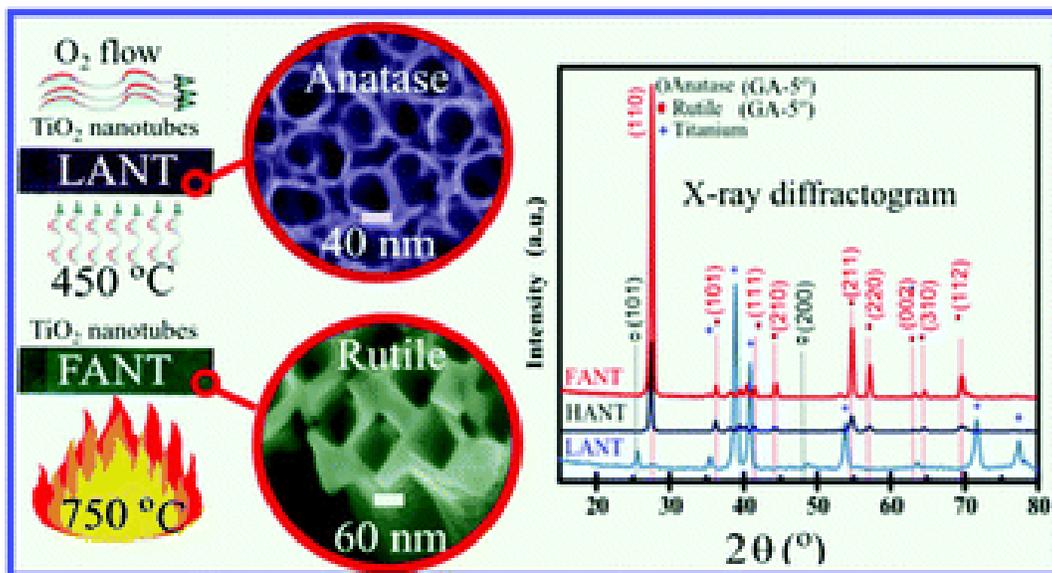
Figure 2- 5 Flame annealing of anatase TiO_2 nanotubes to produce rutile phase TiO_2 nanotubes. FANT mean flame annealed TiO_2 nanotubes and LANT stands for low-temperature annealed TiO_2 nanotubes. Reprinted from [54] with permission from Royal Society of Chemistry.

2.4.2   Oxygen annealing at 750 ºC

I intended to compare the flame annealing process with annealing in furnace to compare the effect of slow temperature ramp-up (and down), and also to evaluate the effect of time at 750 °C. The aqueous TNTAs formed by 750 °C annealing in oxygen atmosphere underwent shape change from pseudo-circular to square as well as phase change to pure rutile. However, the EG TNTAs grown on Si substrate underwent only partial rutile phase transformation and retained their pseudo-circular morphology.

2.5   Characterization of the TNTAs

I characterized the TNTAs by using Zeiss Sigma field emission scanning emission Microscopy (FESEM), XRD (using a Bruker D8 Discover instrument with a sealed Cu tube X-ray source, and Raman spectroscopy (using a Nicolet Almega-XR Raman spectrometer by applying a 532nm laser source). While FESEM is a powerful imaging to nanostructural morphology TiO_2 nanotubes, XRD outputs detailed information about crystalline phase content. Raman spectroscopy is widely used for analyzing crystalline phase content via phonon dispersion. Quantatively, Raman spectroscopy is also applied to determine effect of crystalline size and lattice strain on phonon lifetime.

2.5.1   TNTAs grow on Ti foil

TNTAs after anodization were annealed 450 °C annealed TNTAs (called LANTs), 450 °C followed by propane flame annealed TNTAs (called FANTs), and 750 °C annealed TNTAs (called HANTs). LANTs, FANTs and HANTs were all formed by anodization in aqueous electrolytes, and FESEM images of the same are shown in Figure 2- 6. It is clearly evident fromthe images that annealing in propane flame (FANTs) and at

750 °C (HANTs) lead to square shaped pore morphology. That change in their shape may

be due to excessive strainbecause of large amount of additional heat.
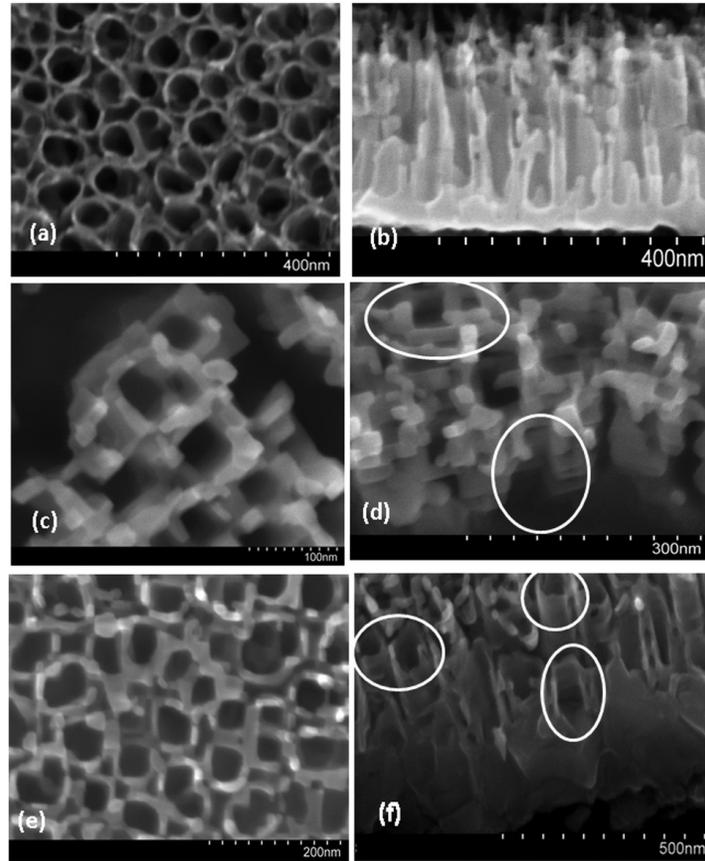
Figure 2- 6 FESEM image of LANTs (a and b), HANTs (c and d) and FANTs (e and f). The circular marks indicate square section from cross-section. Reprinted from [54] with permission from Royal Society of Chemistry.
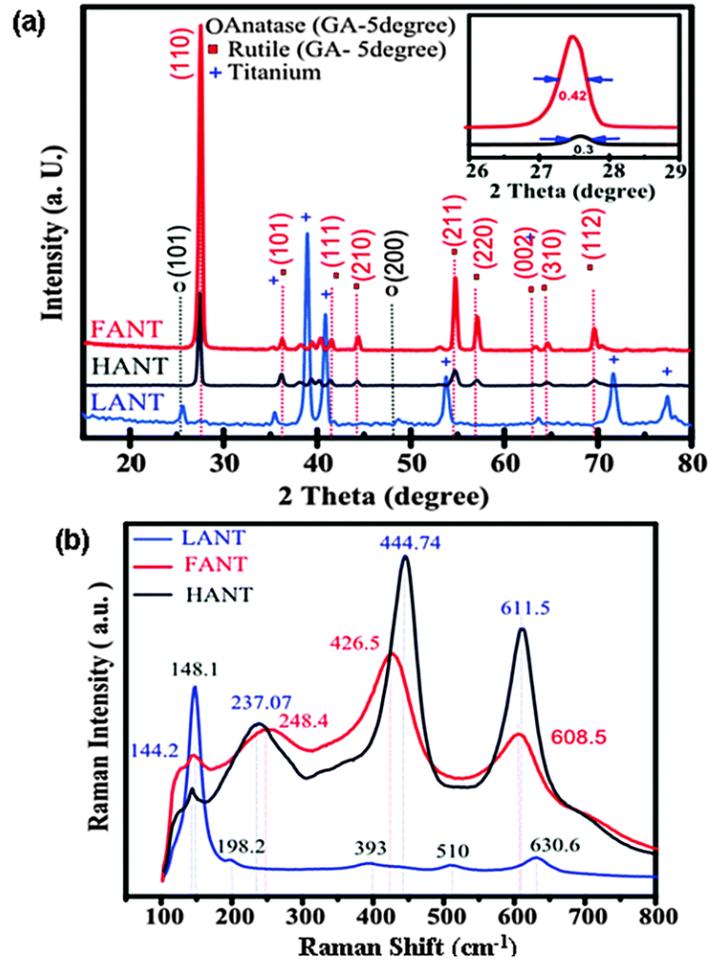
Figure 2- 7 XRD and Raman spectra of LANTs, HANTs and FANTs. Reprinted from [54] with permission from Royal Society of Chemistry.

XRD spectra for flame annealed TNTAs (FANTs) and 750 °C annealed aqueous TNTAs (i.e. HANTs) show dominant peaks at 27.45 °C, which is attributed to the (110) plane of rutile. Absence of anatase specific peak and presence of rutile phase only is confirmed the distinct (110) peak as well as secondary peaks at Bragg angles of 36.1°, 39.2° and 41.2°, denoting rutile planes of (101), (200) and (111), respectively. Peak width at half maximums for the rutile (110) plane are shown in Figure 2- 7 (inset), which

whenincorporated into Scherrer formula (Eq. 1) can yield the crystalline grain size of the rutile phase.

$$s = \frac{K\lambda}{\alpha \cos \theta} \qquad (1)$$

In Eqn. (1), K is assumed to be one, λ is 0.154 nm (i.e. the incident x-ray wavelength), α is the full-width at half maximum (FWHM) of the peaks, and θ is Bragg angle. The obtained sizes using eq. (3) are 21 and 31 nm for FANTs and HANTs, respectively.

It is well-established facts that anatase, due to its tetragonal crystal structure, exhibits six Raman modes, i.e. three E_g (144, 196, and 639 cm^{-1}) modes, two B_{1g} (397 and 519 cm^{-1}) modes and one A_{1g} (513 cm^{-1}) mode. Rutile has four Raman active modes, i.e. one B_{1g} (143 cm^{-1}), one E_g (447 cm^{-1}), one A_{1g} (612 cm^{-1}), and one B_{2g} (826 cm^{-1}). The Raman spectra for FANTs and HANTs show peaks at 144.0 and 147.0 cm^{-1}, respectively. These peaks may be due the anataseE_g mode combined with rutile B_{1g} mode, although contribution of anatase is likely less because of the predominant XRD (110) rutile peak denoting intense rutile crystallization. The secondary rutile Raman modes in HANTS and FANTS are E_g modes (426.5 and 444.74 cm^{-1}for FANTs and HANTs, respectively), A_{1g} modes (608 and 611 cm^{-1} for FANTs and HANTs, respectively). HANTs exhibit blue-shifted peaks compared to FANTs although particle size of the former is bigger than the later. The observed blue shifting may be because of excessive lattice strains and existence of the asymmetric Ti-O bond. Although FANTs also undergo high temperature annealing the high temperature condition is short-lived that likely limits the conversation of thermal energy to shape change and phase transformation only.

2.5.2 TNTAs grown on Si substrate

The building blocks and morphologies of the TNTAs on Si substrate are shown schematically in (Figure 2- 8). FESEM images of the TNTAs are shown Figure 2- 9 a to d). FESEM images illustrate a porous surface with cylindrical profiles (Figure 2- 9c and d) representing TiO_2 nanotube arrays. The nanotubes have an average inner diameter of ~ 80 nm when annealed at 500 °C (Figure 2- 9a), which decreases to ~ 50 nm when annealing temperature is raised to 750 °C (Figure 2- 9c). We attribute the decrease in inner diameters of the nanotubes with increasing annealing temperature to the high-temperature induced outward diffusion of TiO_2 at 750 °C that narrows down the pores. Moreover, we observed an increase in the overall external diameter of the TiO_2 nanotubes than what is observed in nanotubes formed by anodization of Ti foil. The overall tube diameter increase may be explained by the fact that our nanotubes were formed out of sputtered Ti films on Si substrates and also due to our use of high water content EG-based anodization electrolytes.
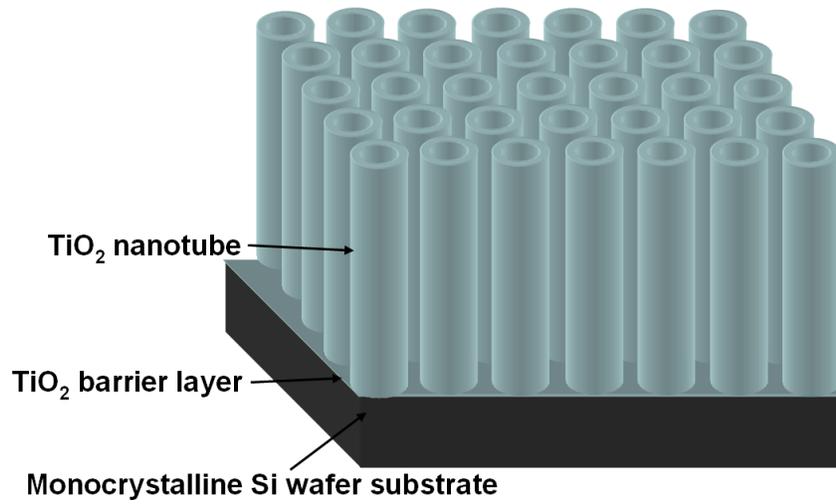
Figure 2- 8Schematicillustration of anodically formed TiO_2 nanotube arrays on a Si wafer substrate.
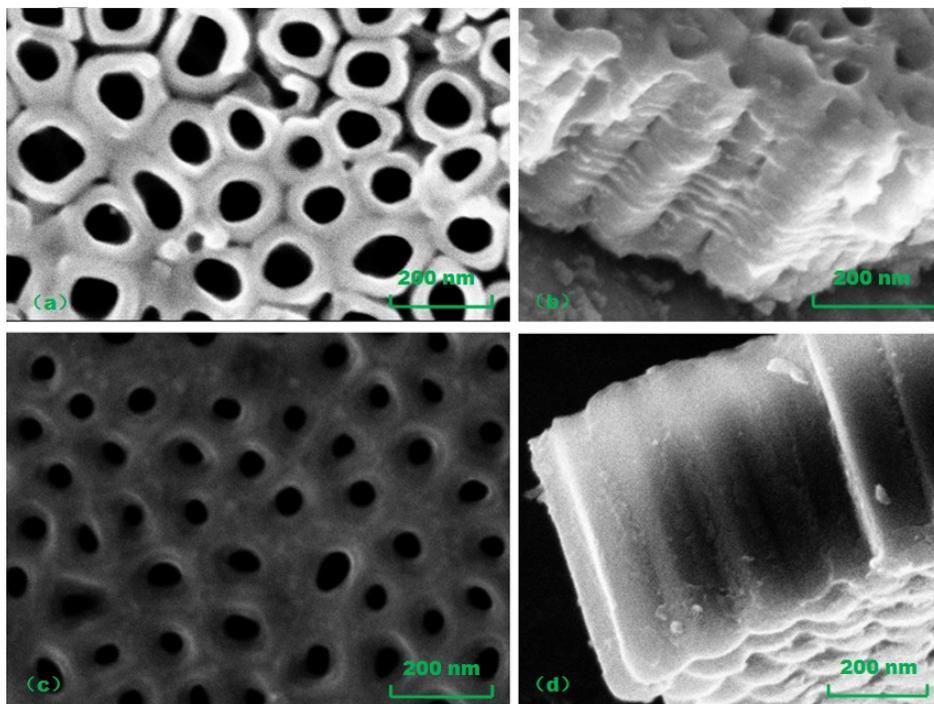
Figure 2- 9 FESEM images of TNTAs anodized at 40 V for 20 min (a) Top view and (b) Cross-section for samples annealed at 500°C for 2.5 hours;(c) Top-view and (d) Cross-section for samples annealed at 750 °C for 2.5 hours.

Figure 2- 10(a) shows XRD patterns of TNTAs after furnace annealing at 500 °C and 750 °C.The initially amorphous as-anodized TNTAs are crystallized by annealing. By comparing the pattern in Figure 2- 10 (a) with the standard pattern of anatase TiO$_2$, we found that all the diffraction peaks of the 500 °C annealed TNTAs (black curve) correspond to the lattice planes of anatase TiO$_2$. No rutile phase is observed for the 500 °C annealed TNTAs. Figure 2- 10 (a) also shows the XRD patterns of TNTAs after furnace annealing at 750 °C for 2.5 hours (red curve) which are transformed into a mixture of anatase and rutile phases as evidenced by reflections corresponding to both phases. These results are in line with prior reports on the structural transformation in

TNTAs upon annealing at elevated temperatures[26, 55]. Crystallite sizes for anatase and rutile grains are determined from the anatase (101) and rutile (110) peaks (Figure 2- 11 (a)) by using Scherrer equation (eq. (1)). The size of anatase grains in the TNTAs annealed at 500 °C is 17.39 nm and same in TNTAs annealed at 750 °C is 35.82 nm. The size of rutile grains in TNTAs annealed at 750 °C is 29.88 nm. The intensities of rutile (110) and anatase (101) peaks in XRD pattern of TNTAs annealed at 750 °C was used to estimate the percentage of rutile (p)[56], according to the following relationship:

$$p = \frac{Ir}{0.884.Ia + Ir} \quad (2)$$

In Eqn. (2), I_a is the intensity of anatase (101) peak and I_r is the intensity of rutile (110) peak. Using Eqn. (2), p is 29 % in our TNTAs annealed at 750 °C.

Raman spectra for the TNTAs annealed at 500 °C and 750 °C are shown in Figure 2-10 (b). The presence of anatase phase alone in the 500 °C annealed TNTAs (blue curve in Figure 2- 10 (b)) is also confirmed by Raman peaks near 143, 395, 519 and 633 cm^{-1} corresponding to the E_g, B_{1g}, B_{1g} and E_g modes respectively[57]. The aforementioned peaks also appear in the Raman spectrum of TNTAs 750 °C annealed TNTAs (red curve in Figure 2- 10 (b)) at 141, 394, 519 and 635 cm^{-1} corresponding to the E_g, B_{1g}, B_{1g} and E_g modes respectively. There is an additional E_g peak at 198 cm^{-1} due to greater degree of anatase crystallization at 750 °C. As indexed, the peak positions and Raman modes pre-dominantly correspond to anatase, although a low intensity rutile E_g peak at 440 cm^{-1} is observed[58-59]. It may be assumed that the intense peak at 141 cm^{-1} has contributions from both anataseE_g and rutile B_{1g} modes but such contributions may be ruled based on

the annealing temperature of 750 °C[60]. Therefore, the 141 cm^{-1} Raman peak in the 750 °C annealed TNTAs may be considered anataseE$_g$ Raman mode in its entirety.
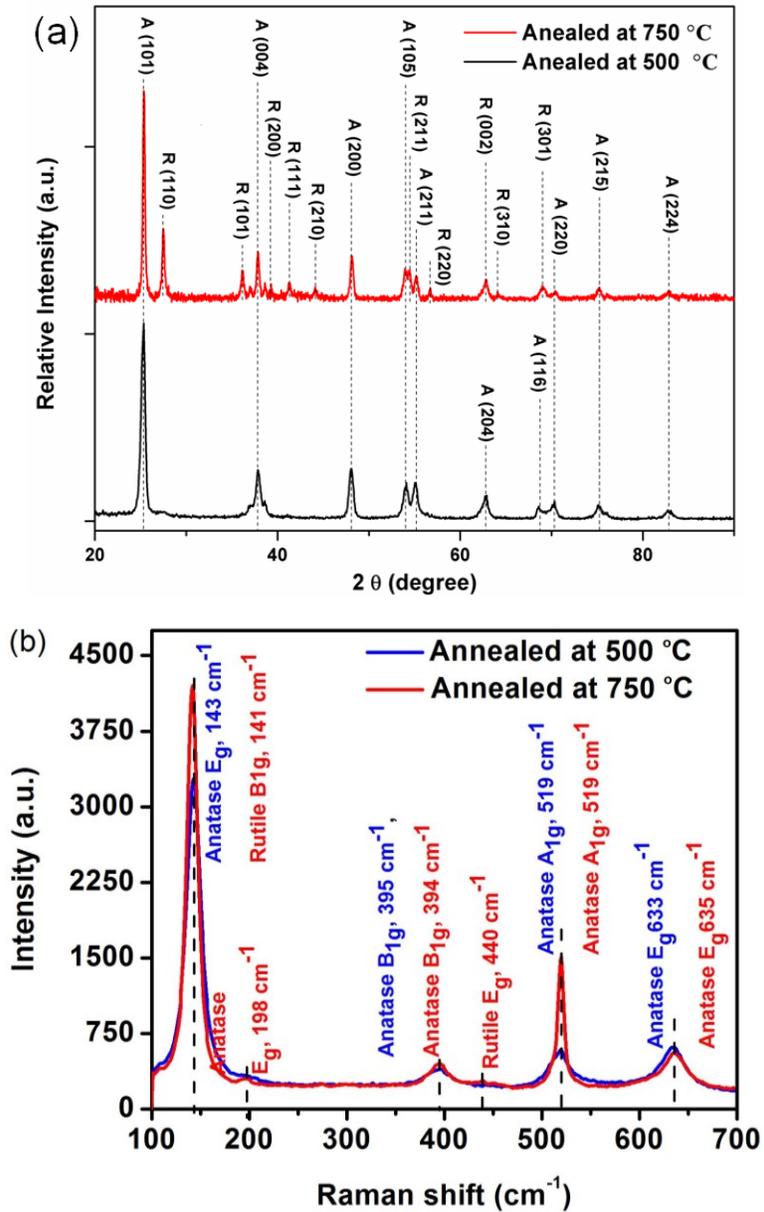
Figure 2- 10 (a) XRD patterns and (b) Raman spectra of TNTAs anodized at 40 V for 20 min and furnace annealed at 500 °C and 750 °C for 2.5 hours.

Unlike larger grains in bulk TiO_2, one-dimensional nanostructures, such TiO_2 nanotubes and nanowires, crystalline grain size are usually small with less than 20 times lattice parameter. At those sizes crystallite grain size of TiO_2 nanotubes, phonon wave function decay to small values near grain boundaries, leading to diminished phonon lifetimes. Furthermore, phonon contribution is from the entire Brillouin zone compared to crystals with larger grain sizes, where phonon dispersion is from center of Brillion zone. Therefore, we have herein analyzed phonon confinement effect in the TNTAs.
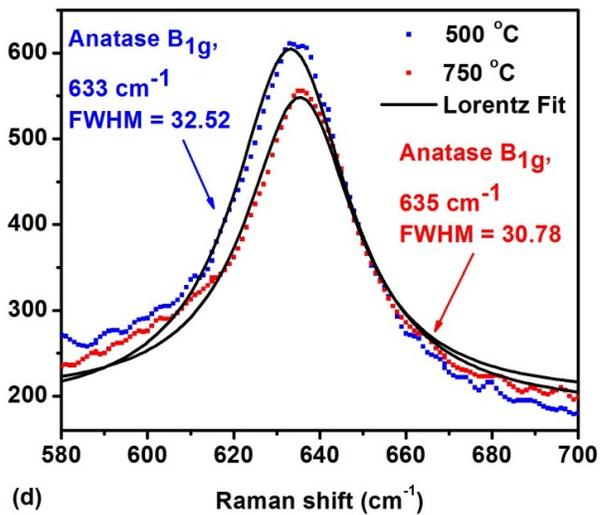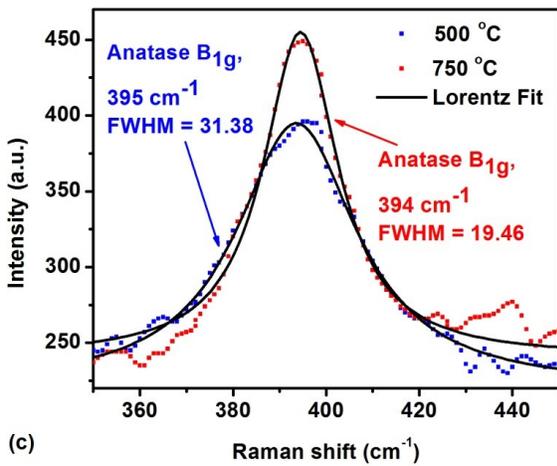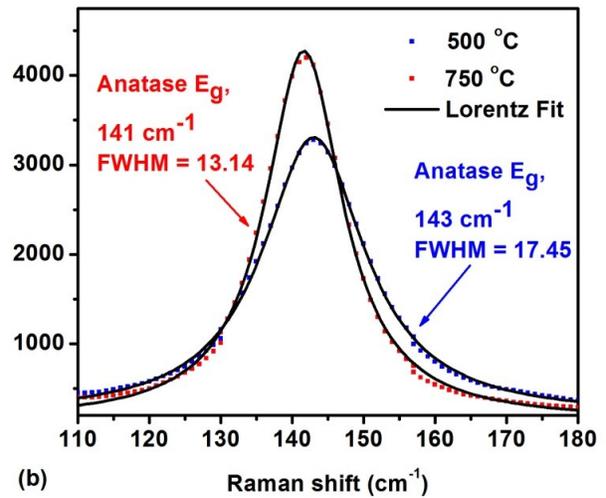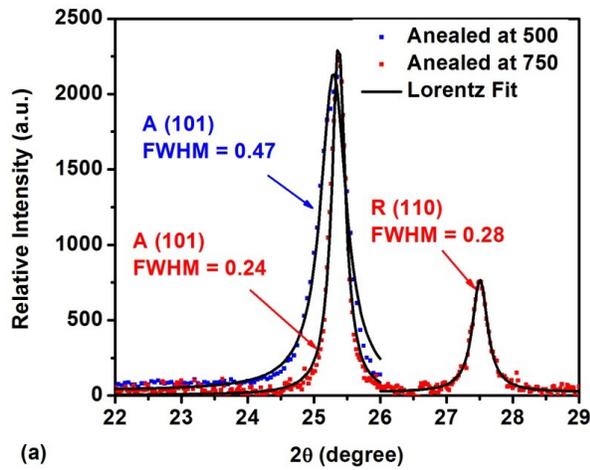
Figure 2- 11 (a) XRD patterns and (b), (c) and (d) are Lorentzian fits of the two E_g and B_{1g} Raman modes f TNTAs annealed at 500 and 750 °C.

Generally, the phonon confinement effect in TiO_2nanocrystals is analyzed from asymmetric broadening and shifting of E_g peaks of anatase, which is usually the most intense Raman peak and the one that is affected by crystalline grain size. The other Raman modes in anatase (the A_{1g} peak, the two B_{1g} and the two E_g peaks) also undergo broadening and blue-shifting as a result of particle size, but to a lesser extent[61]. To analyze the phonon confinement effect, we performed Lorentzian fitting of the main peaks.

FWHMs were obtained from Lorentzian model fits of the Raman peaks (Figure 2- 11 (b), (c), and (d)).Table 2- 1 shows the FWHM, phonon lifetime and crystallite sizes of the TNTAs annealed at 500 and 750 °C. The narrower and sharper Raman peaks may be due to their intensification due to annealing that is indicated by their narrower FWHMs and longer phone lifetimes, which are close for those reported for Eg (144 cm^{-1}) mode for TiO_2 nanotubes[61-62]. The FWHMs and phonon lifetimes for the B_{1g} and high frequency E_g modes match well with a similar Gaussian confinement model for the E_g (144 cm^{-1}), B_{1g} (397 cm^{-1}) and E_g (639 cm^{-1}) peaks are 7.5, 20 and 20 cm^{-1}, respectively[61]. The relatively blue-shifted E_g peak of the 500 °C annealed TNTAs is likely because of their smaller (101) anatase crystallite size compared to same in 750 °C annealed TNTAs. The anatase B_{1g} peak at 395 cm^{-1} for the 500 °C annealed TNTAs lies closer the bulk TiO_2 value (397 cm^{-1}[62]), than the same at 394 cm^{-1} for 750 °C annealed TNTAs, implying consistency with the shifts in low frequency E_g peaks. Raman peaks

for the high frequency B_{1g} and E_g modes for anatase in the TNTAs are red-shifted from their bulk values of 519 and 639 cm^{-1}, respectively.

We applied a time-energy uncertainty relation (Eqn. (3)) to obtain phonon lifetimes for the Raman peaks of the TNTAs[63].

$$\frac{\Delta E}{\hbar} = \frac{1}{\tau} \quad (3)$$

In Eqn. (3), ΔE is the FWHM, $\hbar = 5.3 \times 10^{-12}$ cm^{-1}.s, and τ is the phonon lifetime. τ for the 395 cm^{-1} B_{1g} Raman peaks, thus obtained, are 0.12 and 0.19 ps for TNTAs annealed 500 °C and those annealed at 750 °C, respectively. The shorter phone lifetime for TNTAs annealed at 500 °C is consistent with the phenomenon of phonon wave function decay to low values near grain boundaries of small grains.

TNTAs annealed at 500 °C			TNTAs annealed at 750 °C		
Raman mode	ΔE (cm^{-1})	τ (ps)	Raman peaks	ΔE (cm^{-1})	τ (ps)
AnataseE_g, 143 cm^{-1}	17.45	0.30	Anatase B_{1g} + Rutile B_{1g}, 141 cm^{-1}	13.14	0.40
Anatase B_{1g}, 395 cm^{-1}	31.38	0.17	Anatase B_{1g}, 394 cm^{-1}	19.46	0.27
AnataseE_g, 633 cm^{-1}	34.67	0.15	AnataseE_g, 635 cm^{-1}	30.78	0.17

Table 2- 1 FWHM and phonon lifetime data derived from model for anatase and mixed anatase and rutile

Chapter 3.   Isotropic Optical Measurements on TiO$_2$ Nanotube Arrays

3.1   Introduction

The optical properties of TNTAs materials play an important role in photovoltaic, photocatalytic, and photoelectrochemical devices. Knowing the optical parameters such as refractive index, absorption coefficients, and thin film thickness will contribute to the enhancement of such device performance. By measuring the transmission through a thin film depositedon a transparent substrate like glass, the optical constants can be calculated. Since 1965, the examination of thin films optical properties by analyzing reflectance and transmittance has been studied and reviewed by many researches[64-65]. Light through a thin film material with moderated absorption coefficient will show multiple interferences, as illustrated in Figure 3- 1. In 1983, a method was proposed by R. Swanepoel to determine the refractive index andthickness from the interference fringes of the transmission spectrum with less than 1% error[66].
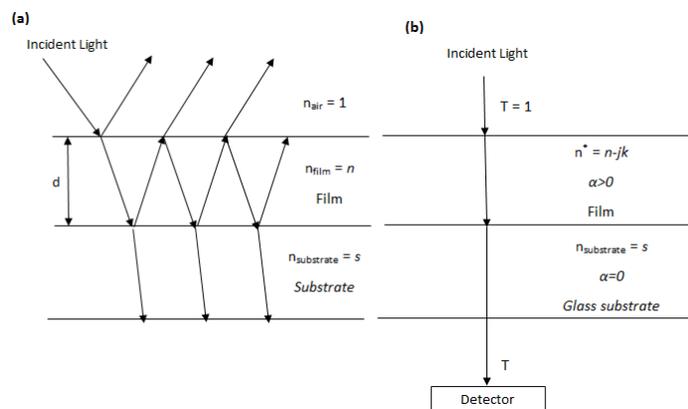
Figure 3- 1Schematic sketch of the typical behavior of light passing through a thin film

on a substrate. （a）demonstration of oblique incidence with the multiple reflections. (b) demonstration of incident beam normal to the film.

The TNTA layer has thin film with thickness d and refractive index n^*=n-ik, where n is the refractive index and k is the extinction coefficient. On a transparent substrate with thickness several orders of magnitude larger than d, refractive index s and extinction coefficient close to zero, the optical properties can be extracted from the transmission measurement. TNTAs can be modeled as an effective medium consistingof TiO_2 with air inclusions. Since the opticalpath length of light reflected at the TNTA-barrierlayer interface and light reflected at the TTNA-air interface are different,Fabry-Perotinterference fringes[67] are expected in the transmission spectra. A typical transmission spectrum is usually divided into three regions according to their transmittance values, as shown in Figure 3- 2. In the transparent region the measured transmittance is usually larger than 99.99% of the substrate's transmittance value, while in the strong absorption region transmittance is very small and no fringes are shown. Spectrum fringes between the two regions are selected to extract optical parameters.
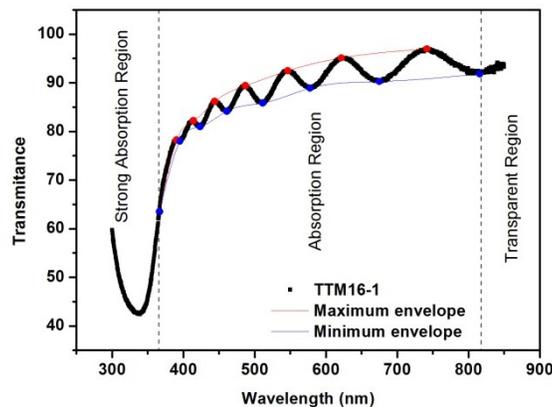
Figure 3- 2 Transmission spectrum a TNTAs sample anodized in 4 vol% water and 0.3

wt% NH4F in EG at 40V.

3.2 Fabrication andCharacterization of TNTAs on glass

500 nm-thick titanium films were deposited onto clean glass substrate using the planar magnetron sputter system with working pressure of 1mTorr, 7mTorr, and 0.7mTorr for sample TTM 16-3, TTM 17-1, and TTM 11-2, respectively.TTM 16-3, TTM 17-1 were deposited under 250°C while TTM 11-2 was deposited under room temperature.Ti deposited substrates were used to form TNTAs by potentiostatic anodization under different conditions (as shown in

Table 3- 1).

	TTM 16-3	TTM 17-1	TTM 11-2
Electrolyte	4 vol% water and 0.3 wt% NH$_4$F in EG	4 vol% water and 0.3 wt% NH$_4$F in EG	5 vol% water and 0.3 wt% NH$_4$F in EG
Anodization Voltage	40V	40V	40V
Anodization Duration	14 min 10 s	41 min 50 s	34 min 28 s
Starting current	26.6 mA/cm^2	28.0 mA/cm^2	24.1 mA/cm^2

Table 3- 1 Anodization condition to fabricated TNTAs on glass substrate in EG

electrolyte.

The anodization current was monitored and recorded using a Keithley 4200-SCS semiconductor parameter analyzer. Samples were rinsed by methanol and dried by nitrogen gun after anodization. Transmission spectra shown inFigure 3- 3were obtained from UV-vis spectroscopic measurements using Perkin Elmer Lambda 900 UV-Vis-NIRspectrophotometer with a beam spot size of 1 cm^2, though the spot can be tuned by using a aperture. Transmittance for a blank glass substrate was also measured for refractive index calculation.
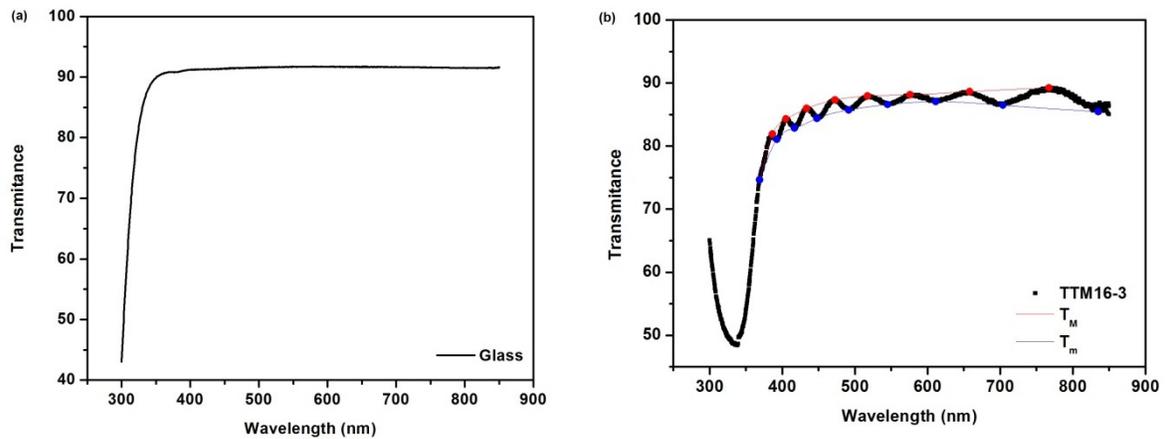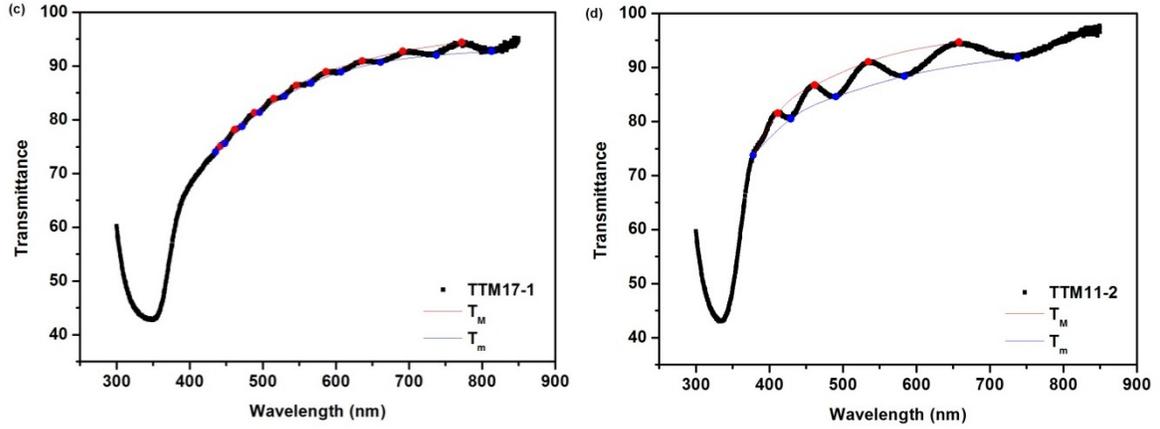
Figure 3- 3 Transmittance spectra measured from (a) blank glass, (b) TNTAs TTM 16-3, (c) TNTAs TTM 17-1, and (d) TNTAs TTM 11-2, and construction of envelopes in the TNTAs transmittance spectra fringes.

3.3   Analysis of Transmission Spectra

Two envelopes connecting all the local maxima and minima are constructed, noted as T_M and T_m. Transmittance is a function of wavelength λ, refractive index n, absorbance α, and film thickness d. Hence the refractive index can be expressed as

$$n = [N + (N^2 - s^2)^{1/2}]^{1/2} (1),$$

where

$$N = 2s \left[\frac{T_M - T_m}{T_M T_m} \right] + \frac{s^2 + 1}{2} .$$

The calculated refractive indices are shown in Figure 3- 4. Inall three measurements, the variations in refractive indices are within 0.1. While in [28], the refractive index was decreasing by 0.15. Compared with the previous result for TNTAs grown on

Kapton[28],the refractive dispersion curves for all three samples didn't show a smoother Cauchy curve. This can be due to the backside reflection of the glass substrate. Surface roughness of glass that may cause void in titanium thin film sputtering may also be a significant factor.
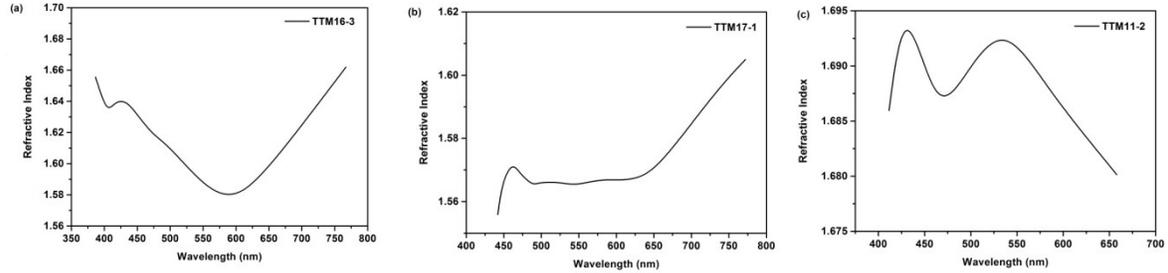
Figure 3- 4Refractive indicesof (a) TNTAs TTM 16-3, (b) TNTAs TTM 17-1, and (c) TNTAs TTM 11-2 obtained using Swanepoel's method.

Film thickness can also be calculated as follows

$$d = \frac{\lambda_1 \lambda_2}{2(\lambda_1 n_2 - \lambda_2 n_1)}(2),$$

where d is the film thickness, i.e. length of the nanotubes, and the refractive indices ofthe film corresponding to adjacent maxima (or minima) atpoints 1 and 2 are given as n_1 at $\lambda_1$and n_2 at λ_2. The average value can be calculated with more thickness values deduced in the same way. The calculated average film thickness for TNTAs sample TTM 16-3, TTM 17-1, and TTM 11-2, are 1.7 μm, 2.7μm, and 1μm, respectively. The results are closed to the actual film thickness.

Compared with the result obtained by Samira et al., all three dispersion patterns in Fig 3.4 did not show smooth Cauchy curve as in their work[29].Such distortion can be explained from two aspects, surface roughness and backside reflection. Since transparent

substrates like glass are reflective on both sides, the beam reflected from the front and back surfaces may interfere with each other, and thus affect the interference pattern detected in the experiment. In addition, Kapton substrates used by Samira et al. are smoother on surface than glass substrates used in our experiment. Microscopic view of the difference from various substrates is shown in Figure 3- 5. Such surface roughness of glass substrates may cause light scattering as well as atomic peening effect[68]. The morphology of TNTAs can be largely affected by non-uniform pitting and nucleation processes caused by the non-uniformities of the Ti film deposited on rough surface. Nevertheless, the reliability of the results can be supported by comparison with the work done byMor, G.K et al.where the TNTAs were also grown on glass substrates[29]. The dispersion curves shown in Figure 3- 4are similar in shape with Figure 1- 5 (d). Obviously shown inFigure 3- 5,silicon substrate provides the best surface uniformity. However, it is not applicable in this chapter as here the discussion is about transparentsubstrates. In Chapter 4, I have discussed about non-transparent substrate, i.e. silicon, which I used to attain the surface uniformity.
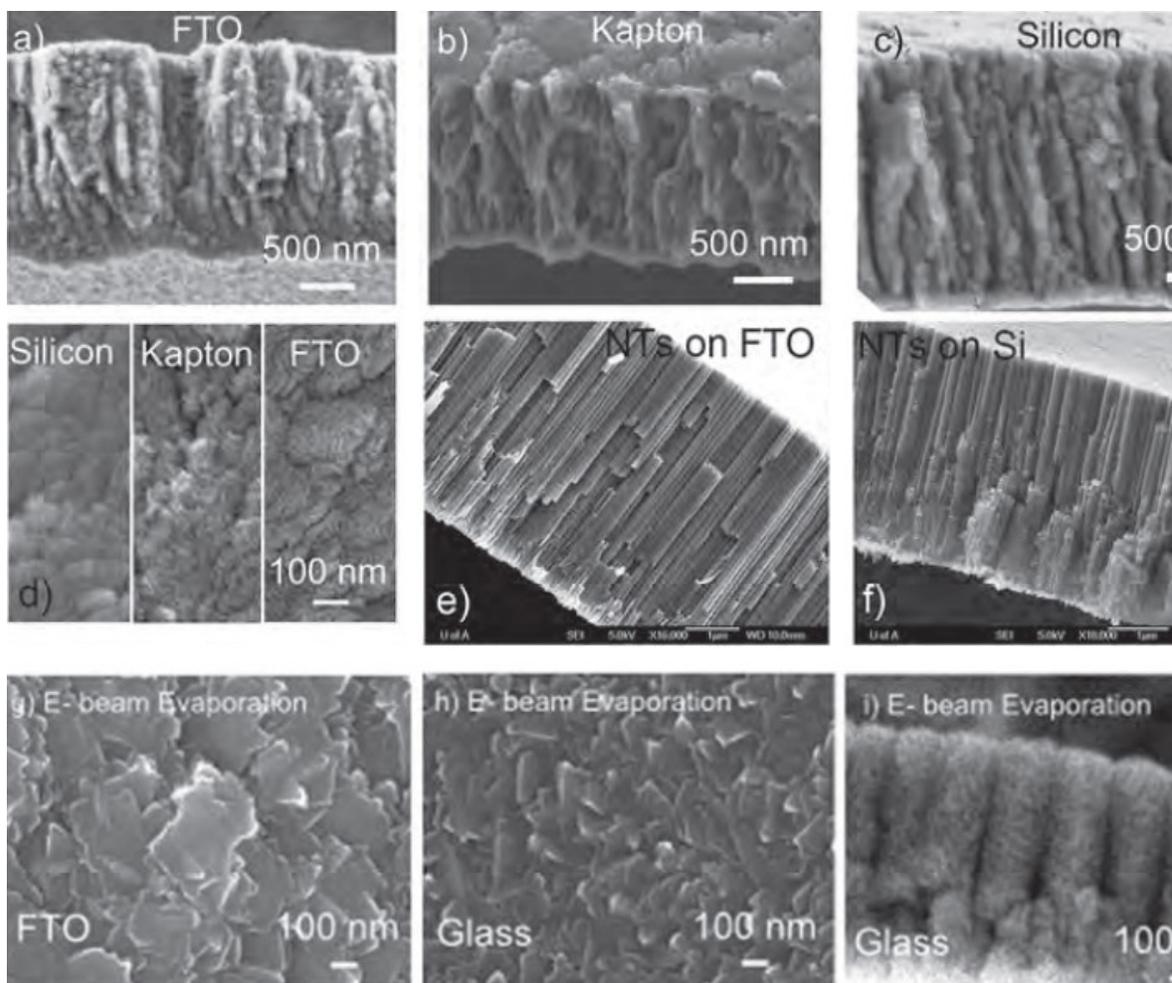
Figure 3- 5 (a–d), (g-i) Cross-sectional and topview of Ti thin films deposited on to glass, FTO coated glass, Kapton and Si wafer substrates respectively; (e, f) ordered TNTAsgrown on substrates shown in (a), (c) and (d).Reprinted from [68]with permission from American Scientific Publishers.

3.4   Summary

In summary, we fabricated TNTAs on glass substrate by performing potentiostatic anodization in EG based electrolyte. As-prepared samples were used for UV-vis spectroscopic measurements. Obtained transmittance spectrawith interferometric fringes were used to extract optical constants. Three different dispersion curves for the refractive indices of TNTAs anodized with different conditions. Swanepeol's method was used to

extract the optical constants. The dispersion curves in Figure 3- 4 showed that the refractive indices for TNTAs on glass substrate were varying from 1.7 to 1.6. Tube lengths were also calculated and were found similar to the actually length. The comparison with previous works indicates that the surface roughness of glass substrate can cause non-physical shaped dispersion curve of refractive indices.

Since TNTAs is an anisotropic material with uniaxial structure, the anisotropic optical properties, will be discussed in Chapter 4.

Chapter 4.   Anisotropic Optical Properties of TiO2 Nanotube Arrays

4.1   Introduction

Anodically formed nanoporous alumina thin films and membranes (AAO) have been used as a platform to fabricate and investigate metamaterials, particularly because of the controllable formation of deep sub-wavelength features by a non-lithographic bottom-up self-organization process[69]. TiO_2nanotube arrays (TNTAs) formed by electrochemical anodization (see Figure 2- 9) constitute a highly ordered and vertically oriented nanostructure similar to AAO but with some important advantages[21]. The much higher refractive index of TiO_2 enables greater refractive index contrast between the TiO_2 matrix and the air inclusions. The wall-thickness and inter-tubular spacing of TNTAs can be tuned within a limited range while the nanotube diameter can be controlled over a much wider range from 10 nm-1000 nm[70-72]. While aluminum oxide is an insulator, both the anatase and rutile forms of titanium dioxide are wide bandgap *n*-type semiconductors, due to which TNTAs are used as the active layer in photocatalysts[73-75], photoelectrodes[76-77] and biosensors [27, 78], and as an electron transport layer in halide perovskite based optoelectronic devices, quantum dots, dye sensitized solar cells[79-80], organic bulk heterojunction solar cells [81-84], batteries and super-capacitors[85-87], memristors[88-89]. Furthermore, self-organized TiO_2 nanotubes have been used to form 1D, 2D and 3D photonic crystals without recourse to lithographic patterning[90-97]. Therefore, TiO_2 nanotube arrays offer a potentially superior platform for both fundamental studies and practical applications of metamaterials.

When a weakly anisotropic uniaxial metamaterial such as AAO is filled with noble metal nanowires, the resulting composite is strongly optically anisotropic with $Re(\varepsilon_{||}) \leq 0$ and $Re(\varepsilon_{\perp}) > 0$ over a certain spectral range, relative to the axis of the cylindrical nanochannels of AAO[98-100]. Such metallodielectricmetamaterials have been used to demonstrate superlens imaging,broadband negative refraction, high Q-factor refractive index sensing of analytes and nonlinear optical enhancement[101-104]. However, metallodielectricmetamaterials are lossy and consequently exhibit limited performance in a wide range of applications due to energy dissipation. In response, there has been a concerted move toward all-dielectric metamaterials which exploit optical anisotropy and/or Mie resonances to generate unusual electromagnetic effects in practical device applications[105-113]. In contrast to lossy surface plasmonpolaritons, Dyakonov-like surface wave packets at the interface between optically anisotropic dielectric nanostructures and an isotropic medium, have shown promise for loss-free subwavelength directional guiding of light [114-118]. TiO$_2$ nanotube arrays are particularly intriguing platforms for all-dielectric metamaterials because they have two distinct sources of anisotropy - (i) morphological and (ii) structural/crystallographic. The source of morphological anisotropy is the uniaxial geometry evident in Figure 2- 3, and is the same as seen in any array of vertically oriented nanopores or nanorods ("so-called wire metamaterial"). The structural anisotropy originates in the tendency of the nano-crystallites constituting the nanotube walls to be either randomly aligned or aligned along the c-axis of tetragonal anatase and rutile lattice structures, depending on the growth conditions[119-120]. Since both anatase and rutile are birefringent crystals, aligned crystallites in the nanotube walls can further amplify the refractive index contrast as

compared to randomly oriented crystallites. While rutile has a large birefringence ($\Delta n = n_e - n_o \sim 0.27$), anatase has a smaller value of Δn (~ 0.07)[121-122]. The optical anisotropy in TNTAs has never been previously measured, and all prior reports have assumed an isotropic permittivity even though TNTAs are clearly uniaxial as seen in Figure 2- 8. In this report, we measured and modeled the anisotropic permittivity of TNTAs on Si wafer substrates.

4.2   Experimental

250 nm-thick titanium (purity >99.999%) films were deposited onto piranha-cleaned n-type <111> oriented silicon wafers by using a planar DC magnetron sputtering system. The deposition conditions used were designed to maximize film smoothness by recourse to atomic peening[28]. The lengths of TNTAs are about 600 nm, as shown in Figure 2- 9 (b) and (d), obtained by anodization of the 250 nm Ti layer on Si wafer. The thickness of the TiO$_2$ carpet (i.e. the length of the TNTAs) is dictated by the thickness of the sputter Ti layer which is varied between 50 to 500 nm. Uniformity of the sputtered Ti film will be affected by its thickness, in that the thicker the sputtered film the less uniformity it will have. The refractive indices obtained by effective medium approximations (EMAs), in this work, are independent of thickness. However, considering that longer nanotubes will allow more interaction between light and the nanotube material, which can ensure accuracy of ellipsometry data, the optimal thickness is chosen a balance between the uniformity of the sputtered Ti layer and the accuracy of the ellipsometry output. On the basis of our experiments, we found that 250 nm is the optimal thickness of the Ti layer. TNTAs were fabricated by anodization of Ti thin films in ethylene glycol (EG)-based organic electrolyte containing 0.09 M (0.3 wt %) NH$_4$F and 9 vol% deionized water at a

voltage o 40 V vs. a graphite counter-electrode placed at a distance of 2 cm from the anode. Following anodization, the residual electrolyte and debris were removed by rinsing the samples with methanol. As-prepared TNTAs samples were then annealed in a tube furnace at 500°C for 2.5 hours in flowing oxygen to generate TNTAs conforming to anatase phase. The heating and cooling rates were 5°C min^{-1}. Other as-anodized titania nanotube samples were annealed at 750 °C for 2.5 hours in flowing oxygen to obtain rutile phase TNTAs.

Morphological characterization of the pore diameter, wall-thickness and length of the nanotubes was undertaken using a Zeiss Sigma field emission scanning electron microscope (FESEM). Spectroscopic ellipsometry measurements were carried out, with a variable angle spectroscopic ellipsometer (VASE WoollamInc., USA) in the 600 nm-1200 nm wavelength range with a spectral resolution of 1 nm, and at incident angles from 25° to 75° in steps of 25°. In contrast to the square beam spot of UV-vis, ellipsometry has a circular beam spot with 1 mm diameter. Then three separate sets of data were obtained at each wavelength. A multilayer model was used for data fitting in order to extract the thickness and refractive index of each layer.

4.3   Results and Discussion

The morphologies of the TNTAs were shown and discussed in FESEM images (Figure 2- 9), which illustrate a porous surface with a cylindrical profile (Figure 2- 9 c and d). The nanotubes have an average inner diameter of ~80 nm when annealed at 500 °C (Figure 2- 9 a), and that decreases to ~50 nm when annealing temperature is raised to 750 °C (Figure 2- 9 c). Decrease in inner diameters of the nanotubes by increasing

annealing temperature may be because of high-temperature induced outward diffusion of TiO$_2$ at 750 °C that narrows down the pores. Moreover, we observed an increase in the overall external diameter of the TiO$_2$ nanotubes than that what is observed in nanotubes formed by anodization of Ti foil. The overall tube diameter increase may be explained by the fact we our nanotubes were formed out of sputtered Ti films on Si substrates. It is well established that sputtered Ti films on non-native substrates, such as Si and fluorine doped tin oxide (FTO) glass, can differ from Ti foils in their crystalline orientations of Ti[123]. Differences in crystalline orientation leads to variations in atomic packing densities resulting in variations in anodic oxidation rates of Ti[124-125]. It is quite plausible that our Ti sputtered on Si have significantly higher atomic packing density than the same in Ti foils, resulting in much higher anodic oxidation rate and larger nanotube diameters. The length of TNTAs are about 600 nm (as shown in Figure 2- 9 b and d), obtained by anodization of the 250 nm Ti layer on Si wafer. The thickness of the TiO$_2$ carpet (i.e. the length of the TNTAs) is dictated by the thickness of the sputter Ti layer which is varied between 50 to 500 nm. Uniformity of the sputtered Ti film will be affected by its thickness, in that the thicker the sputtered film the less uniformity it will have. The refractive indices obtained by effective medium approximations (EMAs), in this work, are independent of thickness. However, considering that longer nanotubes will allow more interaction between light and the nanotube material, which can ensure accuracy of ellipsometry data, the optimal thickness is chosen a balance between the uniformity of the sputtered Ti layer and the accuracy of the ellipsometry output. On the basis of our experiments, we found that 250 nm is the optimal thickness of the Ti layer.

For ellipsometric analysis of the optical properties of the TNTAs, a necessary attribute is a highly smooth surface enabling reflectivity measurements. For this reason, atomically smooth monocrystalline silicon wafers were used as the growth substrate since we have previously shown that substrate smoothness has a determinative effect on the uniformity of the resulting nanotubes[123]. Furthermore, sonication and reactive ion etching treatments used to remove anodization debris subsequent to nanotube growth, were deliberately avoided since these treatments also produce a higher dispersion in the heights of the individual nanotubes, which in turn, produces scattering and reduces the reflectivity. The use of fluoride-bearing ethylene glycol-based electrolytes to perform the anodic growth of TNTAs without subsequent cleaning typically results in a higher TiO_2 fill-fraction than aqueous electrolytes where etching is stronger and no re-deposition of TiO_2 occurs.

The high optical quality of the TNTAs used in this study is evident from the observation of interferometric fringes in the specular reflection spectra shown in Figure 4- 1(a). Film thickness can be calculated by using the Tcalc function[126], which is as shown:

$$d = \frac{M\lambda_1\lambda_2}{2(\lambda_1-\lambda_2)\sqrt{n^2-\sin^2\theta}} (1)$$

In Eqn. (1), d is the film thickness, M is the number of peaks in the wavelength range used for calculation, n is the average ordinary refractive index in this case, θ is the angle of incidence with respect to the sample, and λ_1 and λ_2 are the start and end wavelengths in the wavelength range used for calculation. The calculated film thicknesses are 637.81 nm and 774.18 nm for TNTAs annealed at 500 °C and 750 °C respectively. The calculated

result is closed to what is observed from the FESEM images, which is about 600nm, as shown in Figure 2- 9(b) and (d).
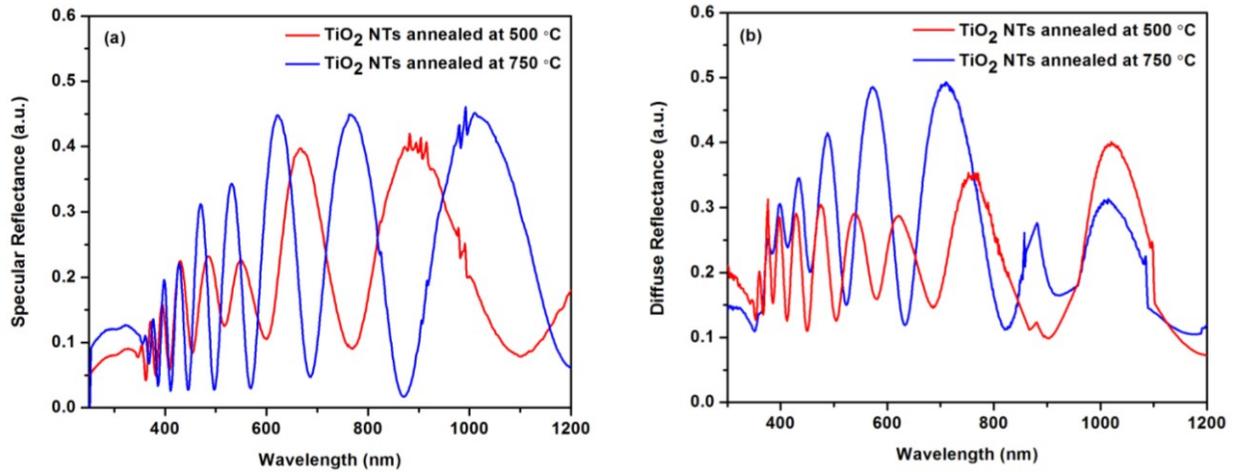
Figure 4- 1(a) Specular and reflection spectra of TNTAs measured in response to unpolarized light incident on the TNTAs at a 20° angle of incidence. The high reflectance values and clear interferometric fringes demonstrate the high optical quality of the TNTA samples. Specular and (b) diffuse reflection spectra of TNTAs measured in response to unpolarized at normal incidence.

Figure 4- 1(b) shows the diffuse reflection spectra, which has very similar patterns and values with the specular reflection pattern in Figure 4- 1. With the difference between specular and diffuse reflectance being very small, we can safely put the assumption that the scattering effect is negligible in this experiment.

When the feature size of the structure, in this case the wall thickness (~20nm) is much smaller than the wavelength of incident light (hundreds of nanometers), effective medium approximations (EMAs) can be used to obtain the effective optical properties of nanocomposites. For a two-component medium such as shown in Figure 2- 8,Bruggeman (BR) and Maxwell-Garnett (MG) are the most frequently used EMAs. While BR theory

applies for all filling fractions of the two components, MG theory is only valid for dilute systems wherein the volumetric filling fraction of the guest material in the host matrix is low. Since the titania component has a high filling fraction in the nanotube arrays as shown in Figure 2- 9, we decided to use the BR approximation for uniaxial media according to which the ordinary (ε_o) and extraordinary (ε_e) components of the effective permittivity are given by [127]

$$\frac{(1-f)\left(\varepsilon_{air}-\varepsilon_o\right)}{\left(\varepsilon_{air}+\varepsilon_o\right)/2}+\frac{f\left(\varepsilon_{TiO_2}-\varepsilon_o\right)}{\left(\varepsilon_{TiO_2}+\varepsilon_o\right)/2}=0 \qquad (2)$$

$$\frac{(1-f)\left(\varepsilon_{air}-\varepsilon_e\right)}{\varepsilon_e}+\frac{f\left(\varepsilon_{TiO_2}-\varepsilon_e\right)}{\varepsilon_e}=0 \qquad (3)$$

Eqns. (2) and (3) highlight the importance of first estimating the volumetric fill fraction f of TiO_2 in the air matrix in the TNTAs. f depends on the diameter, wall-thickness and packing of the nanotubes, and can vary substantially for different growth conditions e.g. varied anodization and etching conditions. For the TNTAs in Figure 2- 8, f is given by [128-129]

$$f=\frac{\dfrac{2(a-b)}{a}-\left(\dfrac{(a-b)}{a}\right)^2}{\dfrac{2\sqrt{3}}{\pi}\left[1+\left(\dfrac{\beta-2a}{2a}\right)^2\right]} \qquad (4)$$

where a is the outer radius of the nanotubes, b is the inner radius and β is the center-to-center spacing as shown in Figure 4- 2. Applying Eqn. (4) to the dimensions of the

TNTAs in this study (see Figure 2- 9), we found $f = 0.62$ for the anatase-phase TNTAs and $f = 0.68$ for anatase-rutile mixed phase TNTAs.
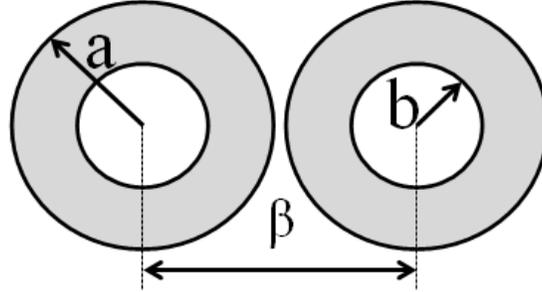
Figure 4- 2 Geometry of the nanotube architecture used in effective medium calculations.

The BR expressions in Eqns (2) and (3) for the effective optical permittivity do not take into account the cylindrical symmetry of the two-component uniaxial medium constituted by the TNTAs. For an array of vertically oriented, parallel cylinders and cylindrical shells (assumed infinite in length), the effective permittivities of the nanocomposite $\varepsilon_{eff}^{\parallel}$ parallel to, and $\varepsilon_{eff}^{\perp}$ perpendicular to the axes of the cylinders are given by [130]

$$\varepsilon_{eff}^{\parallel} = \varepsilon_{air} + f(\varepsilon_{TiO_2} - \varepsilon_{air}) \qquad (5)$$

$$\varepsilon_{eff}^{\perp} = \varepsilon_{air}\left(1 + 2f\frac{\Delta_{eff}}{[1 - f\Delta_{eff}]}\right) \quad (6)$$

In (5) and (6),

$$\Delta_{eff} = \frac{\varepsilon_{air} - \varepsilon_{TiO_2}}{\varepsilon_{air} + \varepsilon_{TiO_2}}(a^2 - b^2)/a^2 - \left(\frac{\varepsilon_{air} - \varepsilon_{TiO_2}}{\varepsilon_{air} + \varepsilon_{TiO_2}}\right)^2 b^2 \quad (7)$$

With $\varepsilon_{eff}^{\parallel}$ the same as ε_e, and $\varepsilon_{eff}^{\perp}$ the same as ε_o. The extinction coefficient k (imaginary part of the complex refractive index) of the TNTAs is assumed to be negligibly small, which is a valid assumption for wavelengths larger than 600 nm, since the sub-bandgap absorption of TNTAs due to defects and impurities typically extends only to ~ 600 nm[131]. Since the optical extinction of TiO_2 inclusive of the Urbach tail can be ignored in the wavelength region of interest (600 nm − 1200 nm), the effective refractive index n_{eff} is given by the square-root of the effective optical permittivity. The effective ordinary and extraordinary refractive indices of TNTAs calculated using the published values for the permittivity of polycrystalline TiO_2[132],and the equations for a Bruggeman medium (BR) and a medium containing vertically oriented, parallel cylindrical inclusions (CYL), are shown in Figure 4- 3.
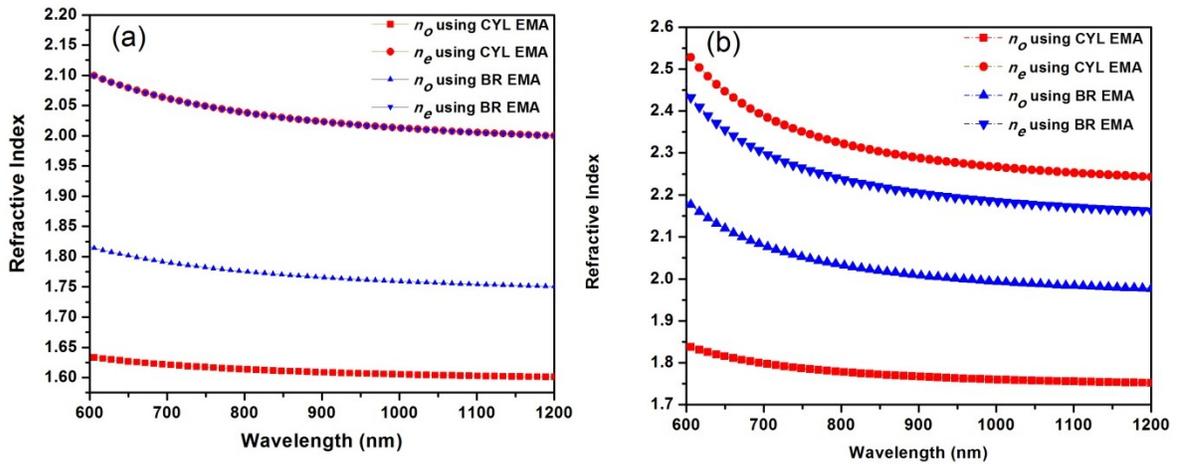
Figure 4- 3 Anisotropic refractive index of TNTAs constituted by (a) Anatase-phase TiO_2 and (b) Rutile-phase TiO_2, calculated using the BR and CYL effective medium approximations, see Eqns (1) through (6).

The rutile phase of TiO_2 has a much higher refractive index than anatase, a fact reflected in Figure 4- 3 in the values of both the refractive index for extraordinary rays n_e and the refractive index for ordinary rays n_o,being higher for rutile-phase TNTAs compared to anatase-phase TNTAs. Figure 4- 3 indicates n_e to be significantly higher than n_o for all the cases considered, and such a high directional refractive index contrast due to anisotropy is desirable for all-dielectric metamaterials as previously discussed. However, the calculated birefringence ($\Delta n = n_e - n_o$) is smaller when using the BR effective medium approximation.

Variable angle spectroscopic ellipsometry (VASE) [133] is a powerful non-destructive technique for optical and electronic characterization of materials. It measures the change in polarization state of transmitted or reflected light from a sample surface. Variable angle measurements help to filter multiple solutions of the ellipsometric equation set, and help choose the true solution[134], while the spectroscopic measurements enhance the information content by providing the dispersion of optical parameters[135]. The interaction of polarized light with a medium is described by the complex Fresnel reflection coefficients r_s and r_p(for s- and p- polarized light respectively) which link the amplitude and phase of the reflected light to the incident light. The measured quantity (a ratio of the Fresnel coefficients) is usually expressed as a function of Ψand Δ[133]

$$\frac{r_p}{r_s} = \tan \Psi \ e^{i\Delta} \qquad (8)$$

The refractive index (n) and extinction coefficient (k) which are analytically related to these two parameters (Ψandλ) can thus be measured using ellipsometry at an oblique

incidence. By applying a numerical analysis based on a mathematical model of the optical dispersion of the medium, parameters such as the thickness and optical constants of a certain layer of the multilayer sample can be determined.

The collected data is shown in Figure 4- 4, which are dispersion patterns of the measured quantities $\Psi$and Δ. The determination of the optical parameters is based on choosing the appropriate model that enables the best fitting of these dispersion curves. A three-layer model was first built for data fitting. The bottom layer in this model was the monocrystalline silicon substrate. The second layer consisted of the oxide barrier layer which is transparent in the measurement wavelength range. Therefore the Cauchy model which is an empirical relationship between the refractive index and optical wavelength for transparent materials[136] was selected to describe the optical dispersion of the oxide barrier layer. The top layer in the three-layer model was the TNTA layer, which was first considered to be isotropic, so that it could be represented by the Cauchy model and parameters extracted for use as intelligent starting parameters in later fitting models incorporating anisotropy. The generated Ψ and Δdispersions are shown in Figure 4- 4(a) and (b). We can see from the dispersion that the generated delta dispersion matched the experimental data qualitatively, however, the generated Ψ data did not fit the experimental data very well. Uniaxial anisotropy was then added to the top Cauchy layer. Following the anisotropic fitting procedure provided by J. A.Woollam[137], the fit improved compared to the isotropic model. The generated Ψ and Δ dispersions for the anisotropic model are shown in Figure 4- 4(c) and 7(d) where both the generated dispersions show a good match with the experimental data.
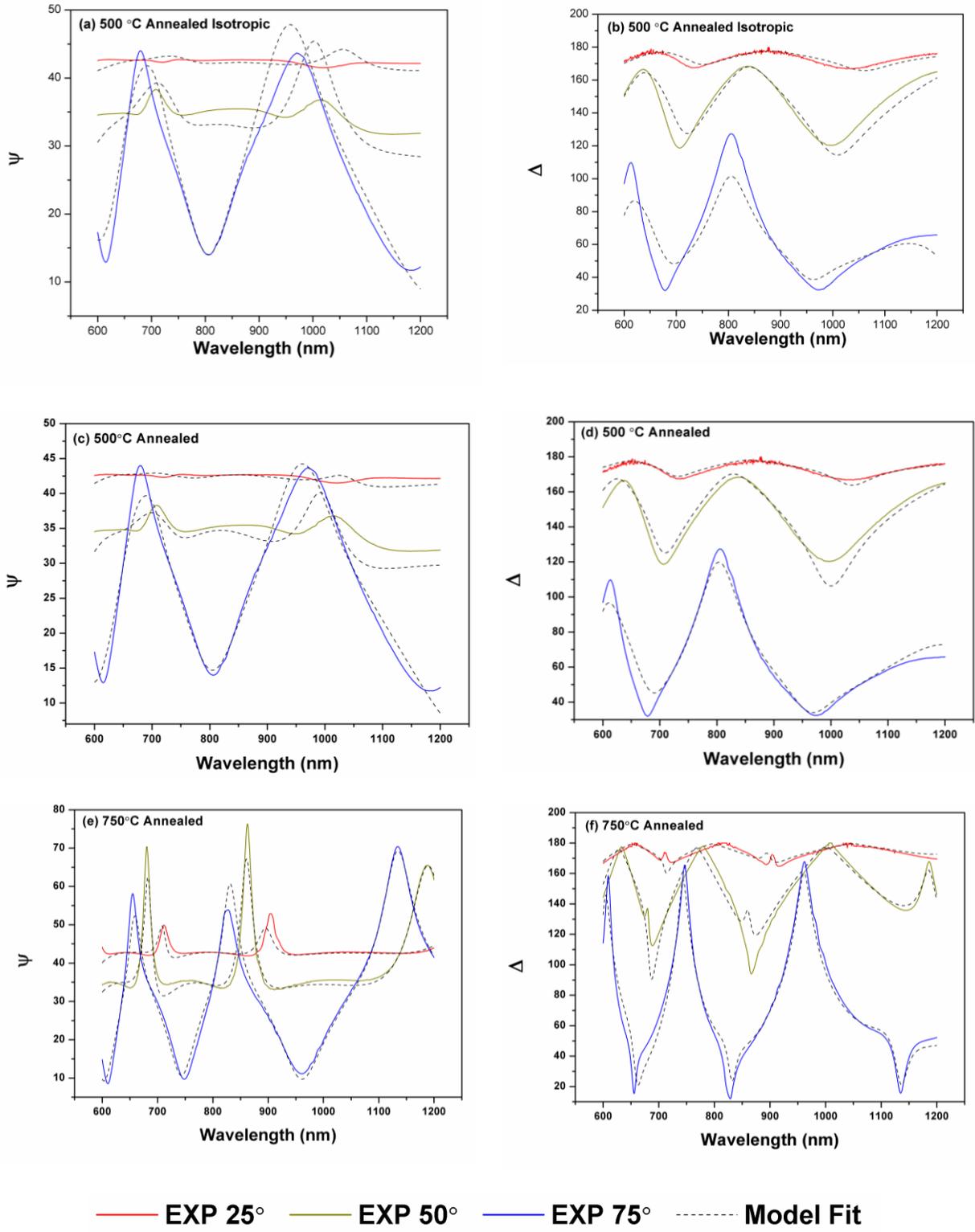
Figure 4- 4Ellipsometric dispersion patterns including measured experimental data (solid lines) and generated curves from best-fit models (dotted lines) for three different angles of

incidence. Panels (a), (c) and (e) correspond to anatase-phase TNTAs while panels (b), (d) and (f) correspond to rutile+anatase mixed phase TNTAs. While panels (a) and (b) show the results of isotropic fits to the Ψ and Δ spectra of anatase-phase TNTAs, panels (c) and (d) show the anisotropic fitting data for anatase-phase TNTAs. (e)and (f) show the experimental data and anisotropic curve fits for rutile+anatase mixed phase TNTAs.

The uniaxial fit indicated a layer thickness of 440.9 nm for the TNTAs which is very close to the length of the nanotubes measured in the FESEM image (Figure 2- 9 **d**). Figure 4- 5 (a) shows the ordinary (n_o) and extraordinary (n_e) refractive indices of the anatase-phase TNTA layer determined from experimental data, as a function of wavelength. Both n_o and n_e for anatase-phase TNTAs show the same trend as bulk anatase[121-122], but are smaller in magnitude due to the presence of air. The dispersion of the birefringence (Δn) was calculated andis displayed in Figure 4- 5(c), which shows that the anatase-phase TNTAs are a positive birefringent material wherein the birefringence decreases with increasing wavelength. The same procedure was repeated rutile+anatase mixed phase TNTAs obtained by annealing at 750 °C, and the generated Ψ and Δ dispersions are shown in Figure 4- 4 (e) and (f). The extracted refractive indices and birefringence dispersion rutile+anatase mixed phase TNTAs are shown in Figure 4- 5 (c) and(d), and found to be slightly higher than those of the pure anatase TNTAs. The magnitude of the birefringence of the anatase-phase TNTAs in this study (0.06 - 0.13) is higher than that of bulk anatase single crystals - which indicates the role of the nanotube geometry in achieving a higher optical anisotropy. On the other hand, the magnitude of the birefringence of the mixed-phase TNTAs in this study (0.06 - 0.15) is lower than that of bulk rutile single crystals due to the lack of phase-purity. The experimentally

determined values for the refractive index and birefringence of the TNTAs in Figure 4- 5 match better with the corresponding values calculated from BR effective medium approximations rather than the CYL EMA.
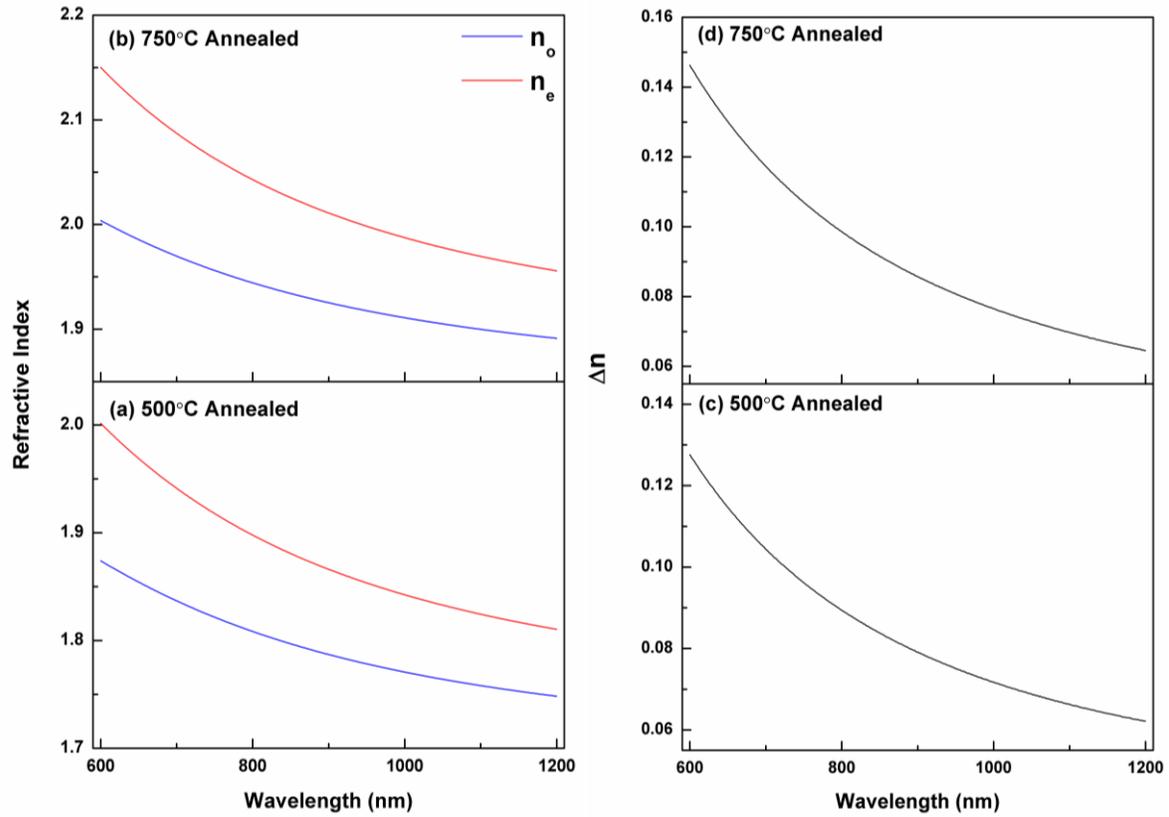
Figure 4- 5 Ordinary and extraordinary refractive indices dispersion pattern of (a) anatase TNTAs and(b) rutile+anatase mixed-phase TNTAs. And birefringence dispersion patterns for (c) anatase TNTAs and(d) rutile+anatase mixed-phase TNTAs.

The TNTAs act as photonic crystals which exhibit strong interaction with light. The average refractive index of TNTAs is approximately 2, hence when the incidence light is in the visible region, the wavelength of light interacted with the nanostructure will be ~300nm. From Figure 2- 9, we can see that the TNTA structures have the periodicity around 150nm, which meets the requirement for a periodic dielectric material to be

photonic crystal that its periodicity should be on the order of half of the light wavelength. Light diffraction can also be observed visually from the sample surface.

4.4   Summary

In summary, we obtained the refractive indices for the propagation of ordinary and extraordinary rays in titania nanotube arrays.   We fabricated smooth TNTAs with specularly reflecting surfaces on a silicon wafer substrate and investigated their anisotropic optical properties using variable angle spectroscopic ellipsometry. A uniaxial Cauchy model was used to extract optical constants from the experimental data. Comparison of FESEM imaging and ellipsometry analysis permitted us to deduce the thickness of the anatase NTAs layer to be 441 nm, and that of the mixed phase anatase+rutile TNTAs to be 570 nm. Both anatase-phase and mixed phase TNTAs exhibited positive birefringence. In the visible-near infrared spectra range of 600 nm−1200 nm, the ordinary refractive indices of anatase-phase TNTAs showed a decreasing trend from 1.87 to 1.73, and 2.00 to 1.87 for mixed phase TNTAs while the extraordinary refractive indices showed a similar trend decreasing from 2.00 to 1.85 for anatase-phase TNTAs and 2.15 to 1.97 for mixed phase anatase+rutile TNTAs.

Chapter 5.   Conclusion and Future Works

5.1   Summary and results

This chapter summarizes: the process protocols used to form the rutile phase TNTAs on Ti foil and also on Si substrate; key characteristics of the TNTAs that are inferred from their XRD patterns ad Raman spectra; and isotropic and anisotropic optical properties of the TNTAs grown on Si substrate.

5.1.1   Fabrication of rutile phase TNTAs

Anodically formed TNTAs were obtained onglass, silicon, and native substrate (i.eTi foil). Both (EG)-based organic electrolyte containing 0.09 M (0.3 wt %) NH$_4$F and 9 vol% deionized water, and aqueous electrolytes containing 1 vol% hydrofluoric acid, and 8 vol% acetic acid were used in potentiostatic anodization. Crystallized TNTAs were obtained by performing annealing in a tube furnace with flowing oxygen. Anatase phase TNTAs was formed at temperatures close to 400 ºC. Rutile phase becomes dominant with temperature above 700 ºC in TNTAs grown on Ti foil, and it is 29 % of the mixed anatase and rutile TNTAs that are formed on Si substrate, by 750 ºC annealing. TNTAs grown on Ti foils form 100 % rutile as well as square pore morphology (as opposed to pseudo-circular pore morphology in regular TNTAs), when they were annealed in tube furnace at 450 C for 30 minutes followed by propane flame annealing.

XRD and Raman spectroscopy confirmed the existence of pure rutile phase in high temperature annealed TNTAs anodized in both aqueous and EG based electrolyte. However, TNTAs formed on Si substrates that are anodized in EG based electrolyte partly rutile crystallized. Raman spectra of the TNTAs are consistent with XRD data in

that Raman modes distinct to rutile appeared in the flame annealed and high temperature annealed TNTAs, which are grown on Ti foils using aqueous electrolyte. Predominance of anatase Raman modes are observed for 750 °C annealed mixed phase TNTAs formed on Si substrate. Phonon confinement effect was analyzed by quantitative analysis of theRaman spectra, which revealed a distinct crystallite-size related broadening of Raman peaks ofthe TNTAs annealed at 500 °C.

5.1.2 Isotropic Optical Properties of TNTAs

Swanepeol's method was used to extract the refractive indices and film thickness of TNTAs fabricated on glass substrate. By measuring three TNTAs in different anodization conditions, I have obtained that their refractive index dispersions with wavelength are between 1.7 and 1.55. Theobtained refractive index dispersions were compared with the results in previous work. Their tube lengths are varying from 1 to 2.6 μm in the visible spectra range of 350 nm−800 nm depending on different anodization conditions.

5.1.3 Anisotropic Optical Properties of TNTAs

Anisotropic refractive indices of ordinary and extraordinary rays were extracted using variable angle spectroscopic ellipsometry. By fitting the ellipsometry data with a uniaxial Cauchy model, I have found that both anatase-phase and mixed phase TNTAs exhibited positive birefringence. In the spectra range of 600 nm−1200 nm, the ordinary refractive indices of anatase-phase and mixed phased TNTAs was varying from 1.87 to 1.73, and 2.00 to 1.87, respectively, while the extraordinary refractive indices showed a

similar trend decreasing from 2.00 to 1.85 and 2.15 to 1.97 for anatase-phase TNTAs and mixed phase anatase+rutile TNTAs, respectively. Such results were compared and found acceptable with effective media approximation using Bruggeman model and Maxwell-Garnett model.

5.2   Future Work

Using the feature of TNTAs by different surface functionalization schemes, high performance photocatalysisapplications can be envisioned. The optical properties can be changed with decorating TNTAs with different materials. Such work will significantly enhance the performances of photocatalysis and light harvesting devices.

There is a strong motivation to construct TiO_2-noble metal composites such as Ti-Au nanotubes which can provide localized surface plasmon resonance induced improvement in function and performance in optical through the enhancement of local electromagnetic fields. Nanostructured gold can harvest visible and near-infrared light, and generate and inject hot electrons into TiO_2[138-139]. Electrochemical anodization can be used on stack layered titanium-gold thin films to synthesize gold embedded titania nanotubes. In such materials and designs, I can applyboth ellipsometry and transmittance spectra fringes measurements to investigate the optical properties of nanotubes formed on Ti-Au co-deposited substrates.

Titanium nitride also exhibits interesting optical properties, like localized surface plasmon resonance and surface enhanced Raman scattering.It is also a material that can be used in functionalizing TNTAs, and the resulting nanocomposites can be applied for potentially enhanced performance in applications, such as photocatalysis[140].TiNcan be deposited onto TNTAs by using atomic layer deposition (ALD), and isotropic

ellipsometrycan be performed to investigate optical properties of TiN coated TNTAs. Such results can be compared with effective medium approximation.

Reference

1.   Jamieson, J.C., et al., *PRESSURE-TEMPERATURE STUDIES OF ANATASE, BROOKITE RUTILE AND TIO2 (II)-A DISCUSSION*. 1969, MINERALOGICAL SOC AMER 1015 EIGHTEENTH ST, NW SUITE 601, WASHINGTON, DC 20036. p. 1477-&.

2.   Beltran, A., L. Gracia, and J. Andres, *Density functional theory study of the brookite surfaces and phase transitions between natural titania polymorphs*. The Journal of Physical Chemistry B, 2006. **110**(46): p. 23417-23423.

3.   Anthony, J.W., et al., *Handbook of mineralogy, mineralogical society of America, Chantilly, VA 20151-1110, USA*. 2011, ed.

4.   Moellmann, J., et al., *A DFT-D study of structural and energetic properties of TiO2 modifications*. Journal of physics: condensed matter, 2012. **24**(42): p. 424206.

5.   Kern, P., P. Schwaller, and J. Michler, *Electrolytic deposition of titania films as interference coatings on biomedical implants: Microstructure, chemistry and nano-mechanical properties*. Thin Solid Films, 2006. **494**(1): p. 279-286.

6.   Kato, K., et al., *Morphology of thin anatase coatings prepared from alkoxide solutions containing organic polymer, affecting the photocatalytic decomposition of aqueous acetic acid*. Journal of materials science, 1995. **30**(3): p. 837-841.

7.   Topuz, B.B., et al., *The effect of tin dioxide (SnO 2) on the anatase-rutile phase transformation of titania (TiO 2) in mica-titania pigments and their use in paint*. Dyes and Pigments, 2011. **90**(2): p. 123-128.

8.   Hattori, A., et al., *A promoting effect of NH4F addition on the photocatalytic activity of sol-gel TiO2 films*. Chemistry Letters, 1998. **27**(8): p. 707-708.

9.   Fox, M.A. and M.T. Dulay, *Heterogeneous photocatalysis*. Chemical reviews, 1993. **93**(1): p. 341-357.

10.   Sopyan, I., et al., *Highly efficient TiO2 film photocatalyst. Degradation of gaseous acetaldehyde*. Chemistry letters, 1994. **23**(4): p. 723-726.

11.   Augustynski, J., *The role of the surface intermediates in the photoelectrochemical behaviour of anatase and rutile TiO2*. Electrochimica Acta, 1993. **38**(1): p. 43-46.

12. Jellison Jr, G., et al., *Spectroscopic ellipsometry of thin film and bulk anatase (TiO 2).* Journal of Applied Physics, 2003. **93**(12): p. 9537-9541.

13. Jellison, G., F. Modine, and L. Boatner, *Measurement of the optical functions of uniaxial materials by two-modulator generalized ellipsometry: rutile (TiO 2).* Optics letters, 1997. **22**(23): p. 1808-1810.

14. Jaroenworaluck, A., et al., *Characteristics of silica-coated TiO2 and its UV absorption for sunscreen cosmetic applications.* Surface and Interface Analysis, 2006. **38**(4): p. 473-477.

15. Liu, B. and E.S. Aydil, *Growth of oriented single-crystalline rutile TiO2 nanorods on transparent conducting substrates for dye-sensitized solar cells.* Journal of the American Chemical Society, 2009. **131**(11): p. 3985-3990.

16. Wang, Y.-Q., et al., *Rutile-TiO2 nanocoating for a high-rate Li4Ti5O12 anode of a lithium-ion battery.* Journal of the American Chemical Society, 2012. **134**(18): p. 7874-7879.

17. Ge, M., et al., *Template-free synthesis and photocatalytic application of rutile TiO2 hierarchical nanostructures.* Industrial & Engineering Chemistry Research, 2011. **50**(11): p. 6681-6687.

18. Hanaor, D.A. and C.C. Sorrell, *Review of the anatase to rutile phase transformation.* Journal of Materials science, 2011. **46**(4): p. 855-874.

19. Zallen, R. and M. Moret, *The optical absorption edge of brookite TiO 2.* Solid State Communications, 2006. **137**(3): p. 154-157.

20. Zhou, P., et al., *Bicrystalline TiO 2 heterojunction for enhanced organic photodegradation: engineering and exploring surface chemistry.* RSC Advances, 2017. **7**(27): p. 16484-16493.

21. Shankar, K., *TiO2 Nanotube Arrays: Growth and Application*, in *Encyclopedia of Nanotechnology*. 2012, Springer. p. 2742-2755.

22. Ge, M., et al., *A review of one-dimensional TiO 2 nanostructured materials for environmental and energy applications.* Journal of Materials Chemistry A, 2016. **4**(18): p. 6772-6801.

23. O'regan, B. and M. Grfitzeli, *A low-cost, high-efficiency solar cell based on dye-sensitized.* nature, 1991. **353**(6346): p. 737-740.

24. Adachi, M., et al., *Formation of titania nanotubes with high photo-catalytic activity.* Chemistry letters, 2000. **29**(8): p. 942-943.

25. Varghese, O.K., et al., *Extreme changes in the electrical resistance of titania nanotubes with hydrogen exposure.* Advanced Materials, 2003. **15**(7-8): p. 624-627.

26. Kar, P., et al., *Rutile phase n- and p-type anodic titania nanotube arrays with square-shaped pore morphologies.* Chemical Communications, 2015. **51**(37): p. 7816-7819.

27. Mun, K.S., et al., *A Stable, Label-free Optical Interferometric Biosensor Based on TiO2 Nanotube Arrays.* Acs Nano, 2010. **4**(4): p. 2070-2076.

28. Farsinezhad, S., et al., *Transparent Anodic TiO$_2$ Nanotube Arrays on Plastic Substrates for Disposable Biosensors and Flexible Electronics.* Journal of Nanoscience and Nanotechnology, 2013. **13**(4): p. 2885-2891.

29. Mor, G.K., et al., *Transparent highly ordered TiO2 nanotube arrays via anodization of titanium thin films.* Advanced Functional Materials, 2005. **15**(8): p. 1291-1296.

30. Chen, C.-Y., et al., *Giant optical anisotropy of oblique-aligned ZnO nanowire arrays.* Optics express, 2012. **20**(3): p. 2015-2024.

31. Hodgkinson, I.J., et al., *Measurement of the principal refractive indices of thin films deposited at oblique incidence.* JOSA A, 1985. **2**(10): p. 1693-1697.

32. Wang, H., *Reflection/transmission measurements of anisotropic films with one of the principal axes in the direction of columnar growth.* Journal of Modern Optics, 1995. **42**(3): p. 497-505.

33. Heavens, O., *Optical properties of thin films.* Reports on Progress in Physics, 1960. **23**(1): p. 1.

34. Chen, H.-Y., et al., *Gallium nitride nanorod arrays as low-refractive-index transparent media in the entire visible spectral region.* Optics express, 2008. **16**(11): p. 8106-8116.

35. Michailowski, A., et al., *Highly regular anatase nanotubule arrays fabricated in porous anodic templates.* Chemical physics letters, 2001. **349**(1): p. 1-5.

36.	Chen, Q., et al., *Trititanate nanotubes made via a single alkali treatment.* Advanced materials, 2002. **14**(17): p. 1208-1211.

37.	Li, H., et al., *Templated synthesis of TiO2 nanotube macrostructures and their photocatalytic properties.* Nano Research, 2015. **8**(3): p. 900-906.

38.	Mor, G.K., et al., *A review on highly ordered, vertically oriented TiO 2 nanotube arrays: fabrication, material properties, and solar energy applications.* Solar Energy Materials and Solar Cells, 2006. **90**(14): p. 2011-2075.

39.	Prakasam, H.E., et al., *A new benchmark for TiO2 nanotube array growth by anodization.* The Journal of Physical Chemistry C, 2007. **111**(20): p. 7235-7241.

40.	Roy, P., S. Berger, and P. Schmuki, *TiO2 nanotubes: synthesis and applications.* Angewandte Chemie International Edition, 2011. **50**(13): p. 2904-2939.

41.	Macak, J.M., et al., *TiO2 nanotubes: Self-organized electrochemical formation, properties and applications.* Current Opinion in Solid State and Materials Science, 2007. **11**(1): p. 3-18.

42.	Regonini, D., et al., *Effect of heat treatment on the properties and structure of TiO2 nanotubes: phase composition and chemical composition.* Surface and interface analysis, 2010. **42**(3): p. 139-144.

43.	Taveira, L., et al., *Initiation and growth of self-organized TiO2 nanotubes anodically formed in NH4F/(NH4) 2SO4 electrolytes.* Journal of the Electrochemical Society, 2005. **152**(10): p. B405-B410.

44.	Thompson, G., et al., *Anodic oxidation of aluminium.* Philosophical Magazine B, 1987. **55**(6): p. 651-667.

45.	Thompson, G., *Porous anodic alumina: fabrication, characterization and applications.* Thin solid films, 1997. **297**(1): p. 192-201.

46.	Su, Z. and W. Zhou, *Formation mechanism of porous anodic aluminium and titanium oxides.* Advanced materials, 2008. **20**(19): p. 3663-3667.

47.	Regonini, D., et al., *Anodised TiO2 nano-tubes: voltage ramp influence on the nano-structured oxide and investigation of phase changes promoted by thermal treatments.* physica status solidi (a), 2007. **204**(6): p. 1814-1819.

48.   Farsinezhad, S., A.N. Dalrymple, and K. Shankar, *Toward single-step anodic fabrication of monodisperse TiO2 nanotube arrays on non-native substrates.* physica status solidi (a), 2014. **211**(5): p. 1113-1121.

49.   Kar, P., et al., *Formation and stability of anatase phase of phosphate incorporated and carbon doped titania nanotubes.* Materials Research Bulletin, 2009. **44**(2): p. 398-402.

50.   Kar, P., *Effect of anodization voltage on the formation of phase pure anatase nanotubes with doped carbon.* Inorganic Materials, 2010. **46**(4): p. 377-382.

51.   Allam, N.K. and C.A. Grimes, *Room temperature one-step polyol synthesis of anatase TiO2 nanotube arrays: photoelectrochemical properties.* Langmuir, 2009. **25**(13): p. 7234-7240.

52.   Varghese, O.K., et al., *Crystallization and high-temperature structural stability of titanium oxide nanotube arrays.* Journal of Materials Research, 2003. **18**(1): p. 156-165.

53.   Zhang, Y., et al., *Optical anisotropy in vertically oriented TiO2 nanotube arrays.*

54.   Kar, P., et al., *Rutile phase n-and p-type anodic titania nanotube arrays with square-shaped pore morphologies.* Chemical Communications, 2015. **51**(37): p. 7816-7819.

55.   Varghese, O.K., et al., *Crystallization and high-temperature structural stability of titanium oxide nanotube arrays.* Journal of Materials Research, 2003. **18**(01): p. 156-165.

56.   Li, W., et al., *Size dependence of thermal stability of Ti O 2 nanoparticles.* Journal of Applied Physics, 2004. **96**(11): p. 6663-6668.

57.   Ohsaka, T., F. Izumi, and Y. Fujiki, *Raman spectrum of anatase, TiO2.* Journal of Raman spectroscopy, 1978. **7**(6): p. 321-324.

58.   Attar, A.S. and Z. Hassani, *Fabrication and Growth Mechanism of Single-crystalline Rutile TiO 2 Nanowires by Liquid-phase Deposition Process in a Porous Alumina Template.* Journal of Materials Science & Technology, 2015. **31**(8): p. 828-833.

59.   Grimes, C.A. and G.K. Mor, *TiO2 nanotube arrays: synthesis, properties, and applications.* 2009: Springer Science & Business Media.

60. Rambabu, Y., M. Jaiswal, and S.C. Roy, *Effect of annealing temperature on the phase transition, structural stability and photo-electrochemical performance of TiO2 multi-leg nanotubes.* Catalysis Today, 2016. **278, Part 2**: p. 255-261.

61. Sahoo, S., A. Arora, and V. Sridharan, *Raman line shapes of optical phonons of different symmetries in anatase TiO2 nanocrystals.* The Journal of Physical Chemistry C, 2009. **113**(39): p. 16927-16933.

62. Lottici, P., et al., *Raman scattering characterization of gel-derived titania glass.* Journal of materials science, 1993. **28**(1): p. 177-183.

63. Di Bartolo, B., *Optical interactions in solids.* 2010: World Scientific Publishing Co Inc.

64. Heavens, O.S., *Optical properties of thin solid films.* 1991: Courier Corporation.

65. Poelman, D. and P.F. Smet, *Methods for the determination of the optical constants of thin films from single transmission measurements: a critical review.* Journal of Physics D: Applied Physics, 2003. **36**(15): p. 1850.

66. Swanepoel, R., *Determination of the thickness and optical constants of amorphous silicon.* Journal of Physics E: Scientific Instruments, 1983. **16**(12): p. 1214.

67. Perot, A. and C. Fabry, *On the application of interference phenomena to the solution of various problems of spectroscopy and metrology.* The Astrophysical Journal, 1899. **9**: p. 87.

68. Farsinezhad, S., et al., *The Morphology of TiO2 Nanotube Arrays Grown from Atomically Peened and Non-Atomically Peened Ti Films.* Journal of Nanoscience and Nanotechnology, 2017. **17**(7): p. 4936-4945.

69. Sousa, C.T., et al., *Nanoporous alumina as templates for multifunctional applications.* Applied Physics Reviews, 2014. **1**(3).

70. Mohammadpour, A. and K. Shankar, *Anodic TiO2 nanotube arrays with optical wavelength-sized apertures.* Journal of Materials Chemistry, 2010. **20**(39): p. 8474-8477.

71. Park, J., et al., *Nanosize and Vitality: TiO2 Nanotube Diameter Directs Cell Fate.* Nano Letters, 2007. **7**(6): p. 1686-1691.

72. Chen, X., et al., *Fabrication of 10 nm diameter TiO2 nanotube arrays by titanium anodization.* Thin Solid Films, 2007. **515**(24): p. 8511-8514.

73. Farsinezhad, S., H. Sharma, and K. Shankar, *Interfacial band alignment for photocatalytic charge separation in TiO2 nanotube arrays coated with CuPt nanoparticles.* Physical Chemistry Chemical Physics, 2015. **17**(44): p. 29723-29733.

74. Kar, P., et al., *Enhanced CH4 yield by photocatalytic CO2 reduction using TiO2 nanotube arrays grafted with Au, Ru, and ZnPd nanoparticles.* Nano Research, 2016. **9**(11): p. 3478-3493.

75. Macak, J.M., et al., *Self-Organized TiO2 Nanotube Layers as Highly Efficient Photocatalysts.* Small, 2007. **3**(2): p. 300-304.

76. Rambabu, Y., J. Manu, and C.R. Somnath, *Enhanced photoelectrochemical performance of multi-leg TiO 2 nanotubes through efficient light harvesting.* Journal of Physics D: Applied Physics, 2015. **48**(29): p. 295302.

77. Dai, G., J. Yu, and G. Liu, *Synthesis and Enhanced Visible-Light Photoelectrocatalytic Activity of p−n Junction BiOI/TiO2 Nanotube Arrays.* The Journal of Physical Chemistry C, 2011. **115**(15): p. 7339-7346.

78. Kar, P., et al., *Ultrahigh sensitivity assays for human cardiac troponin I using TiO2 nanotube arrays.* Lab on a Chip, 2012. **12**(4): p. 821-828.

79. Roy, P., et al., *TiO2 nanotubes and their application in dye-sensitized solar cells.* Nanoscale, 2010. **2**(1): p. 45-59.

80. Bella, F., et al., *Floating, Flexible Polymeric Dye-Sensitized Solar-Cell Architecture: The Way of Near-Future Photovoltaics.* Advanced Materials Technologies, 2016. **1**(2).

81. Qin, P., et al., *Stable and Efficient Perovskite Solar Cells Based on Titania Nanotube Arrays.* Small, 2015. **11**(41): p. 5533-5539.

82. Mohammadpour, A., et al., *Electron Transport, Trapping and Recombination in Anodic TiO$_2$ Nanotube Arrays.* Current Nanoscience, 2015. **11**(5): p. 593-614.

83. Shankar, K., et al., *Effect of device geometry on the performance of TiO2 nanotube array-organic semiconductor double heterojunction solar cells.* Journal of Non-Crystalline Solids, 2008. **354**(19-25): p. 2767-2771.

84.   Kongkanand, A., et al., *Quantum Dot Solar Cells. Tuning Photoresponse through Size and Shape Control of CdSe−TiO2 Architecture.* Journal of the American Chemical Society, 2008. **130**(12): p. 4007-4015.

85.   Xiong, H., et al., *Amorphous TiO2 nanotube anode for rechargeable sodium ion batteries.* The Journal of Physical Chemistry Letters, 2011. **2**(20): p. 2560-2565.

86.   Lu, X., et al., *Hydrogenated TiO2 nanotube arrays for supercapacitors.* Nano letters, 2012. **12**(3): p. 1690-1696.

87.   Lamberti, A. and C.F. Pirri, *TiO 2 nanotube array as biocompatible electrode in view of implantable supercapacitors.* Journal of Energy Storage, 2016. **8**: p. 193-197.

88.   Conti, D., et al., *Memristive behaviour in poly-acrylic acid coated TiO2 nanotube arrays.* Nanotechnology, 2016. **27**(48): p. 485208.

89.   Liu, N., K. Lee, and P. Schmuki, *Reliable Metal Deposition into TiO2 Nanotubes for Leakage-Free Interdigitated Electrode Structures and Use as a Memristive Electrode.* Angewandte Chemie International Edition, 2013. **52**(47): p. 12381-12384.

90.   Lin, J., K. Liu, and X.F. Chen, *Synthesis of Periodically Structured Titania Nanotube Films and Their Potential for Photonic Applications.* Small, 2011. **7**(13): p. 1784-1789.

91.   Yip, C.T., et al., *Direct and Seamless Coupling of TiO2 Nanotube Photonic Crystal to Dye-Sensitized Solar Cell: A Single-Step Approach.* Advanced Materials, 2011. **23**(47): p. 5624-+.

92.   Guo, M., et al., *Design and coupling of multifunctional TiO2 nanotube photonic crystal to nanocrystalline titania layer as semi-transparent photoanode for dye-sensitized solar cell.* Energy & Environmental Science, 2012. **5**(12): p. 9881-9888.

93.   Zhang, X.J., et al., *Photocatalytic Conversion of Diluted CO2 into Light Hydrocarbons Using Periodically Modulated Multiwalled Nanotube Arrays.* Angewandte Chemie-International Edition, 2012. **51**(51): p. 12732-12735.

94.   Zhang, Z.H., et al., *Plasmonic Gold Nanocrystals Coupled with Photonic Crystal Seamlessly on TiO2 Nanotube Photoelectrodes for Efficient Visible Light Photoelectrochemical Water Splitting.* Nano Letters, 2013. **13**(1): p. 14-20.

95.	Zhang, Z.H., et al., *Microwave-Assisted Self-Doping of TiO2 Photonic Crystals for Efficient Photoelectrochemical Water Splitting.* Acs Applied Materials & Interfaces, 2014. **6**(1): p. 691-696.

96.	Kondo, T., et al., *Two-dimensional photonic crystals based on anodic porous TiO2 with ideally ordered hole arrangement.* Applied Physics Express, 2016. **9**(10).

97.	Wang, G., et al., *Anodization fabrication of 3D TiO2 photonic crystals and their application for chemical sensors.* Superlattices and Microstructures, 2016. **100**: p. 290-295.

98.	Dickson, W., et al., *Dielectric-loaded plasmonic nanoantenna arrays: A metamaterial with tuneable optical properties.* Physical Review B, 2007. **76**(11).

99.	Lu, W.T. and S. Sridhar, *Superlens imaging theory for anisotropic nanostructured metamaterials with broadband all-angle negative refraction.* Physical Review B, 2008. **77**(23).

100.	Starko-Bowes, R., et al., *Optical characterization of epsilon-near-zero, epsilon-near-pole, and hyperbolic response in nanowire metamaterials.* Journal of the Optical Society of America B-Optical Physics, 2015. **32**(10): p. 2074-2080.

101.	Yuen, K.P., et al., *Enhancement of optical nonlinearity through anisotropic microstructures.* Optics Communications, 1998. **148**(1-3): p. 197-207.

102.	Tiginyanu, I.M., et al., *Semiconductor sieves as nonlinear optical materials.* Applied Physics Letters, 2000. **77**(15): p. 2415-2417.

103.	Menon, L., et al., *Negative index metamaterials based on metal-dielectric nanocomposites for imaging applications.* Applied Physics Letters, 2008. **93**(12).

104.	Kabashin, A.V., et al., *Plasmonic nanorod metamaterials for biosensing.* Nat Mater, 2009. **8**(11): p. 867-871.

105.	Jahani, S. and Z. Jacob, *All-dielectric metamaterials.* Nature Nanotechnology, 2016. **11**(1): p. 23-36.

106.	Moitra, P., et al., *Realization of an all-dielectric zero-index optical metamaterial.* Nat Photon, 2013. **7**(10): p. 791-795.

107.	Vynck, K., et al., *All-Dielectric Rod-Type Metamaterials at Optical Frequencies.* Physical Review Letters, 2009. **102**(13): p. 133901.

108.   Kallos, E., I. Chremmos, and V. Yannopapas, *Resonance properties of optical all-dielectric metamaterials using two-dimensional multipole expansion.* Physical Review B, 2012. **86**(24): p. 245108.

109.   Ahmadi, A. and H. Mosallaei, *Physical configuration and performance modeling of all-dielectric metamaterials.* Physical Review B, 2008. **77**(4): p. 045104.

110.   Krasnok, A., et al. *Towards all-dielectric metamaterials and nanophotonics.* 2015.

111.   Zhao, Q., et al., *Mie resonance-based dielectric metamaterials.* Materials Today, 2009. **12**(12): p. 60-69.

112.   Tokman, M.D. and M.A. Erukhimova, *Anisotropy-Induced Transparency in Optically Dense Media.* Radiophysics and Quantum Electronics, 2015. **57**(11): p. 821-836.

113.   Corbitt, S.J., M. Francoeur, and B. Raeymaekers, *Implementation of optical dielectric metamaterials: A review.* Journal of Quantitative Spectroscopy and Radiative Transfer, 2015. **158**: p. 3-16.

114.   Polo, J.A. and A. Lakhtakia, *Review of Surface-Wave Propagation at the Planar Interface of a Columnar or Chiral Sculptured Thin Film and an Isotropic Substrate*, in *Nanostructured Thin Films*, G.B. Smith and A. Lakhtakia, Editors. 2008.

115.   Faryad, M. and A. Lakhtakia, *Prism-coupled excitation of Dyakonov-Tamm waves.* Optics Communications, 2013. **294**: p. 192-197.

116.   Zapata-Rodriguez, C.J., et al., *Propagation of Dyakonon Wave-Packets at the Boundary of Metallodielectric Lattices.* Ieee Journal of Selected Topics in Quantum Electronics, 2013. **19**(3).

117.   Takayama, O., D. Artigas, and L. Torner, *Lossless directional guiding of light in dielectric nanosheets using Dyakonov surface waves.* Nat Nano, 2014. **9**(6): p. 419-424.

118.   Miret, J.J., et al., *Nonlocal dispersion anomalies of Dyakonov-like surface waves at hyperbolic media interfaces.* Photonics and Nanostructures-Fundamentals and Applications, 2016. **18**: p. 16-22.

119.   John K, A., et al., *A novel cost effective fabrication technique for highly preferential oriented TiO2 nanotubes.* Nanoscale, 2015. **7**(48): p. 20386-20390.

120. Lee, S., et al., *Crystallographically preferred oriented TiO2 nanotube arrays for efficient photovoltaic energy conversion.* Energy & Environmental Science, 2012. **5**(7): p. 7989-7995.

121. Jellison, G.E., F.A. Modine, and L.A. Boatner, *Measurement of the optical functions of uniaxial materials by two-modulator generalized ellipsometry: rutile (TiO2).* Optics Letters, 1997. **22**(23): p. 1808-1810.

122. Jellison, G.E., et al., *Spectroscopic ellipsometry of thin film and bulk anatase (TiO2).* Journal of Applied Physics, 2003. **93**(12): p. 9537-9541.

123. Farsinezhad, S., A.N. Dalrymple, and K. Shankar, *Toward single-step anodic fabrication of monodisperse TiO2 nanotube arrays on non-native substrates.* physica status solidi (a), 2014. **211**(5): p. 1113-1121.

124. Crawford, G.A. and N. Chawla, *Tailoring TiO 2 nanotube growth during anodic oxidation by crystallographic orientation of Ti.* Scripta Materialia, 2009. **60**(10): p. 874-877.

125. Leonardi, S., et al., *TiO2 nanotubes: interdependence of substrate grain orientation and growth characteristics.* The Journal of Physical Chemistry C, 2011. **116**(1): p. 384-392.

126. Rand, M.J., *Spectrophotometric Thickness Measurement for Very Thin SiO2 Films on Si.* Journal of Applied Physics, 1970. **41**(2): p. 787-790.

127. Wang, H.-y. and C.-g. Fan, *Copper oxide nanostructures: controlled synthesis and their catalytic performance.* Solid State Sciences, 2013. **16**: p. 130-133.

128. Shankar, K., et al., *Highly-ordered TiO2 nanotube arrays up to 220 mu m in length: use in water photoelectrolysis and dye-sensitized solar cells.* Nanotechnology, 2007. **18**(6).

129. Farsinezhad, S., et al., *Amphiphobic surfaces from functionalized TiO2 nanotube arrays.* RSC Advances, 2014. **4**(63): p. 33587-33598.

130. Ninham, B.W. and R.A. Sammut, *Refractive index of arrays of spheres and cylinders.* Journal of Theoretical Biology, 1976. **56**(1): p. 125-149.

131. Ngoc Tai, L., et al., *Optical properties of TiO 2 nanotube arrays fabricated by the electrochemical anodization method.* Advances in Natural Sciences: Nanoscience and Nanotechnology, 2014. **5**(1): p. 015004.

132. Tanemura, S., et al., *Optical properties of polycrystalline and epitaxial anatase and rutile TiO2 thin films by rf magnetron sputtering.* Applied Surface Science, 2003. **212–213**: p. 654-660.

133. Woollam, J.A., P.G. Snyder, and M.C. Rost, *Variable angle spectroscopic ellipsometry: a non-destructive characterization technique for ultrathin and multilayer materials.* Thin Solid Films, 1988. **166**: p. 317-323.

134. Azzam, R.M.A. and N.M. Bashara, *Ellipsometry and Polarized LightNorth-Holland Publ.* Co, Amsterdam, 1977.

135. Flueraru, C., et al., *Sensitivity analysis of ellipsometry applied to uniaxial optical films.* Thin Solid Films, 2000. **379**(1): p. 15-22.

136. Jorgensen, B., *The theory of dispersion models*. 1997: CRC Press.

137. Woollam, J.A., *Guide to using WVASE32*. JA Woollam, 2002.

138. Jiang, W., et al., *Integration of Multiple Plasmonic and Co-Catalyst Nanostructures on TiO2 Nanosheets for Visible-Near-Infrared Photocatalytic Hydrogen Evolution.* Small, 2016.

139. Farsinezhad, S., et al., *Reduced ensemble plasmon linewidths and enhanced two-photon luminescence in anodically formed high surface area Au-TiO2 3D nanocomposites.* ACS Applied Materials & Interfaces, 2016.

140. Wang, L., et al., *Tantalum nitride nanotube photoanodes: establishing a beneficial back-contact by lift-off and transfer to titanium nitride layer.* Electrochemistry Communications, 2016. **72**: p. 27-31.